REPORT
doi:10.26443/seismica.v3i1.729

The First Network of Ocean Bottom Seismometers in the Red Sea to Investigate the Zabargad Fracture Zone

Laura Parisi * [1], **Nico Augustin** [2], **Daniele Trippanera** [3], **Henning Kirk** [4], **Anke Dannowski** [2,5], **Rémi Matrau** [1], **Margherita Fittipaldi** [1], **Adriano Nobile** [1], **Olaf Zielke** [1], **Eduardo Valero Cano** [1], **Guus Hoogewerf** [1], **Theodoros Aspiotis** [1], **Sofia Manzo-Vega** [1], **Armando Espindola Carmona** [1], **Alejandra Barreto** [1], **Marlin Juchem** [1], **Cahli Suhendi** [1], **Mechita C. Schmidt-Aursch** [4], **P. Martin Mai** [1], **Sigurjón Jónsson** [1]

[1]PSE Division, King Abdullah University of Science and Technology, Thuwal, Saudi Arabia, [2]GEOMAR Helmholtz Centre for Ocean Research, Kiel, Germany, [3]Istituto Nazionale di Geofisica e Vulcanologia, Rome, Italy, [4]Alfred-Wegener-Institut, Helmholtz-Zentrum für Polar- und Meeresforschung, Bremerhaven, Germany, [5]K.U.M.-Kiel GmbH, Kiel, Germany

Author contributions: *Conceptualization*: SJ, LP, DT. *Investigation*: LP, HK, AD, RM, MF, AN, OZ, EVC, GH, AEC, APB, MJ, NA, TA, CS, SMV. *Formal Analysis*: LP. *Visualization*: LP, RM. *Writing - original draft*: LP. *Writing - Review & Editing*: LP, NA, DT, AD, AN, EVC, AEC, MSA, PMM, SJ. *Resources*: MSA, PMM, SJ. *Funding acquisition*: LP, DT, SJ. *Project administration*: LP, SJ.

Abstract The slow-spreading Red Sea rift has been the focus of geophysical investigations in the recent past to study the extension of the oceanic crust, the thickness of the sedimentary cover, and the formation of transform faults. Despite these efforts, local seismology datasets remain scarce, limiting their potential contribution to understanding the tectonic evolution of the Red Sea. The Zabargad Fracture Zone, situated in the Northern Red Sea, offsets the rift axis to the East, making it an important tectonic element to better understand the Red Sea rift's formation. To fill the gap of missing seismological observations, we deployed the first passive seismic network in the Red Sea, specifically within the Zabargad Fracture Zone. This network comprised a total of 14 ocean-bottom seismometers (OBS) and four portable onshore broadband seismic stations, positioned on islands and along the Saudi Arabian coast. Our noise analyses revealed that short-period noise (less than 0.2 s) in this region is more pronounced than in many other areas sampled by OBSs, possibly due to intense ship traffic. Within the microseismic noise range, we identified strong contributions from local atmospheric and oceanic sources of noise, which in combination with site effects generated a second peak around 0.2-1 s. At long periods, waveforms may be used for regional and global studies of earthquakes larger than magnitude $M_w \approx 6.7$, and potentially smaller events for an OBS sub-dataset. Finally, we detected a local earthquake with a magnitude $M_w \approx 3.4$, which could have a volcanic or hydrothermal origin.

Production Editor:
Gareth Funning
Handling Editor:
Stephen Hicks
Copy & Layout Editor:
Théa Ragon

Received:
May 1, 2023
Accepted:
March 28, 2024
Published:
May 1, 2024

1 Introduction

The Red Sea is a slow to ultra-slow spreading ridge with an age of less than 14 million years (e.g., Augustin et al., 2021; Delaunay et al., 2023), formed after the break-up of Arabia from Nubia. While many tectonic models of the Red Sea have limited the extent of oceanic spreading to the southern and central Red Sea (e.g., Coleman and McGuire, 1988; Almalki et al., 2015), increasing amount of evidence is pointing to mid-ocean spreading along its entire length (Augustin et al., 2021; Delaunay et al., 2023). An offset of up to ~100 km marks the transition between the northern and central Red Sea. This is usually referred to as the Zabargad Fracture Zone (ZFZ) and extends from Zabargad Island in the South to the southern limit Mabahiss Deep in the North (Figure 1). While there is agreement on the presence of the rift axis in the Mabahiss Deep and Mabahiss Mons (an active volcano located north of the deep, see Figure 1, e.g., Augustin et al., 2021; Delaunay et al., 2023; Fittipaldi et al., 2024), the limits and geological structures of the ZFZ are unclear, mostly because the northern and central Red Sea seafloor is covered by thick sediments (mainly evaporites and Plio-Pleistocene sediments) with the basement exposed at only a few locations. Determining the structure of the ZFZ as one or multiple transform faults, or even as a set of non-transform offsets (NTOs), has important implications for the maximum earthquake size in the ZFZ and thus for seismic and tsunami hazard assessments of coastal communities in this part of the Red Sea.

Accurate earthquake locations are critical for resolving the structure of the ZFZ. However, the existing earthquake catalog from the Saudi Geological Survey exhibits two diffuse clusters of seismicity that are more than 50 km in diameter (Figure 1), with event locations far from being sufficient to image the ZFZ fault system in detail. Moreover, not much is known about large earthquakes in the ZFZ. Only four earthquakes of magnitude larger than 4.5 were instrumentally recorded in the area before the Saudi and Egyptian seismic networks were established and since then only one additional earthquake was large enough (M_w 4.9 in 2015) for focal mechanism determination, showing normal faulting (Figure 1). Strike-slip tectonic movements are also expected in the ZFZ and have been suggested from

*Corresponding author: laura.parisi@kaust.edu.sa

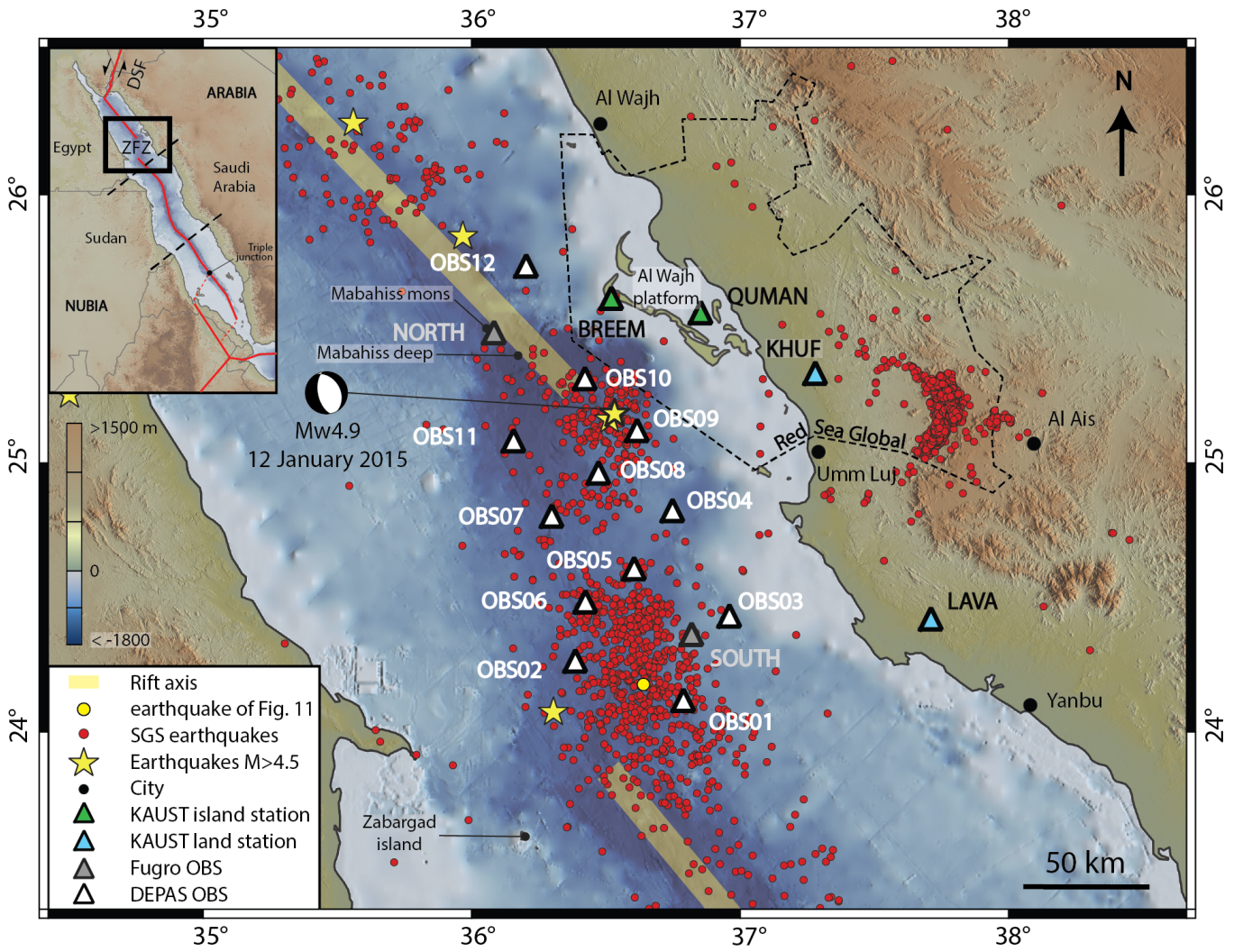

Figure 1 Map of the OBS deployment in the northern Red Sea. The earthquake locations are from the Saudi Geological Survey for 2011-2016, locations of magnitude larger than 4.5 events from IRIS (www.iris.edu, last accessed 5 April 2023), and the focal mechanism of the 12 January 2015, earthquake from the CMT catalog (www.globalcmt.org, last accessed 5 April 2023). Bathymetric data are from GEBCO (www.gebco.net, last accessed 5 April 2023). ZFZ: Zabargad Fracture Zone. DSF: Dead Sea Fault. Dashed lines in the inset separate the northern, central, and southern Red Sea.

tectonic mapping on Zabargad island (Marshak et al., 1992). Furthermore, historical catalogs (El-Isa, 2015; Rehman et al., 2017), while limited, highlight the seismogenic potential of the ZFZ by including reports on two earthquakes of magnitude that could have been as large as M_w 6. Moderate-to-large earthquakes within the ZFZ would threaten neighboring coastal communities on both sides of the Red Sea (Figure 1), in particular on the more populated Saudi coast, e.g., the city of Yanbu with its large petrochemical facilities, the town of Umm Lujj, and Red Sea Global, a major tourist destination under development mostly within the Al Wajh lagoon/platform (Figure 1). The threat may come from the shaking of the weakly consolidated terrains east of the Al-Wajh lagoon and from tsunami waves that could hit the westernmost islands of the same lagoon.

To improve knowledge and understanding of the structure of the ZFZ, we installed the first network of Ocean Bottom Seismometers (OBS) in the Red Sea. We deployed 14 OBSs and four land stations that cover the latitude range 23.5^o-25.5^{o}N (see Figure 1) to establish the temporary ZAFRAN seismic network surrounding the ZFZ to collect broadband seismic data for approximately one year. The primary objective of the deployment is to detect and locate earthquakes to map active faults within the ZFZ. We also plan to construct seismic velocity models of the crust and upper mantle structure to estimate the extent of the oceanic crust and the thickness of the evaporite cover. We will achieve this by utilizing body waves from local and teleseismic events, as well as ambient noise cross-correlations. The results should provide valuable insights into the seismic potential of the ZFZ and, in the broader context, its role in the geological evolution of the Red Sea. Furthermore, the OBS data may help in identifying and characterizing potential active volcanic and hydrothermal sources.

While OBSs enable the collection of data in previously unexplored regions, interpreting and removing seismic noise recorded by OBSs is more challenging compared to noise recorded inland. This complexity arises because sensors deployed inland benefit from insulation against temperature variations, air currents,

and wildlife, due to installations in vaults, direct instrument burial, and other protective measures. In contrast, OBSs are often placed directly on the seafloor without specific protection. The exposure of OBSs to the marine elements may introduce noise in the same frequency band as signals used in seismological investigations (ranging from 40 Hz to 100 s and beyond).

Both OBSs and land seismic stations record the ambient seismic noise that occurs in different frequency bands, corresponding to different noise sources. Seismic noise with wave periods exceeding 1 second generally results from the intricate interplay between the atmosphere, the ocean, and the Earth. The microseismic noise range, commonly defined from 2 to 4 seconds up to 20 seconds (e.g., Stutzmann et al., 2000; Gualtieri et al., 2013), encompasses the secondary microseismic peak, often observed around 7 seconds, and sometimes observed split with an additional peak around 1-2 s (e.g., Parisi et al., 2020). Long-period ambient noise (periods exceeding 10-20 seconds), which typically includes the primary microseismic peak occurring between 10 and 20 seconds, is generated through the interaction of ocean waves with shorelines (e.g., Ardhuin, 2018). Periods exceeding 30 seconds are frequently influenced by infragravity waves originating in coastal regions, capable of propagating back to the open ocean (Ardhuin et al., 2014). Detecting and mitigating this noise from OBS data usually involves analyzing the coherence between pressure and vertical seismic signals (e.g., Janiszewski et al., 2019). Additionally, sea bottom currents, circulating the OBS elements, can introduce noise within this period range, predominantly affecting the horizontal components. In cases of imperfect sensor leveling, this noise may impact the vertical component as well (Crawford and Webb, 2000). The detection and removal of this noise can be achieved by examining the coherence, if present, between the vertical and horizontal components (Crawford and Webb, 2000).

The quality of short-period signals (T<1 s), on the other hand, is less dependent on the sensor performance, but it is crucial for the investigation of local earthquakes and volcanic and hydrothermal activities. Nevertheless, OBS recordings have frequently reported additional sources of seismic signals at short periods, including those generated by ships and marine mammals (e.g., Wilcock, 2012; Trabattoni et al., 2023). Moreover, signals within these short periods may be susceptible to corruption by noise, often generated by sea bottom currents interfering with protruding elements of the OBSs, such as the antenna, beacon, and flags (e.g., Stähler et al., 2018; Essing et al., 2021a).

In this article, we present the deployment of the OBS network in the ZFZ, show examples of the collected data, and highlight notable signals recorded. Furthermore, we provide recommendations for utilizing the dataset, drawing from our data quality assessment and analysis. Lastly, our contribution extends to enhancing the comprehension of the splitting of the secondary microseism peak in the microseismic noise band.

2 The ZAFRAN seismic network

We operated the ZAFRAN seismic network from September 2021 to January 2023 with most of the instruments collecting data from November 2021 to November 2022. The network included 14 broadband OBSs and four onshore portable seismic stations, covering the northern Red Sea in the latitude range 24.0^o-25.8^{o}N and from longitude of 36.5^{o}E to the western coast of Saudi Arabia (Figure 1). The OBS interstation distances ranged from 17 to 42 km whereas the onshore stations were more widely spaced (33-110 km), because they were primarily installed to cross-validate the OBSs waveforms. The station coordinate information can be found in Suppl. Table 1.

2.1 Offshore deployment

The offshore part of the network consisted of 12 Lobster OBSs (stations codes from OBS01 to OBS12) from the DEPAS pool (Alfred-Wegener-Institut Helmholtz-Zentrum für Polar-und Meeresforschung et al., 2017) (Figure 2a and 3), deployed at water depths between 740 m and 1700 m (depths are listed in Suppl. Table 1) and two OBSs designed and deployed by Fugro (station codes NORTH and SOUTH; Figure 2b) at depths of 960 m and 870 m, respectively. The DEPAS OBSs have been used in many OBS deployments around the world (e.g., Geissler et al., 2010; Stähler et al., 2016; Blanck et al., 2020), while the Fugro OBS setup is experimental and has not been tested before. Each DEPAS OBS consisted of a 1.65 x 1.30 m frame equipped with a Güralp CMG-40T-OBS sensor and a SEND MCS data logger hosted in titanium pressure-resistant tubes. The sensor was placed between two floating units, mounted to a metallic plate that sits on an anchor (Figure 3a). To facilitate the import of the OBSs into Saudi Arabia, our setup did not include a hydrophone, in contrast to many OBS deployments. Additional equipment to allow and facilitate the instrument recovery included a floating unit, acoustic releaser, flashlight, radio beacon, flag, and buoy (Alfred-Wegener-Institut Helmholtz-Zentrum für Polar-und Meeresforschung et al., 2017), which is attached to the OBS with about 10 m long and 18 mm thick polypropylene rope (Figure 3b). Given that the rope and buoy have been found to be responsible for high-frequency noise (e.g., Stähler et al., 2018), we deployed six DEPAS OBSs by wrapping the rope and the buoy with a fabric fixed to the releaser and the other six with a free rope and buoy to study the difference in the noise properties. The metallic anchor, allowing each OBS to sink to the seafloor, was locked to the frame through the releaser. The DEPAS OBSs were deployed by free-fall from the research vessels R/V Thuwal (KAUST, Thuwal) and R/V Al Azizi (King Abdulaziz University, Jeddah). Due to the limited deck space on these vessels, the deployment was conducted during two short trips from the KAUST harbor in November 2021.

To recover the DEPAS OBSs, an acoustic release command is sent through the water column to the releaser. The releaser then unlocks the anchor from the OBS, which becomes buoyant enough to float to the sea sur-

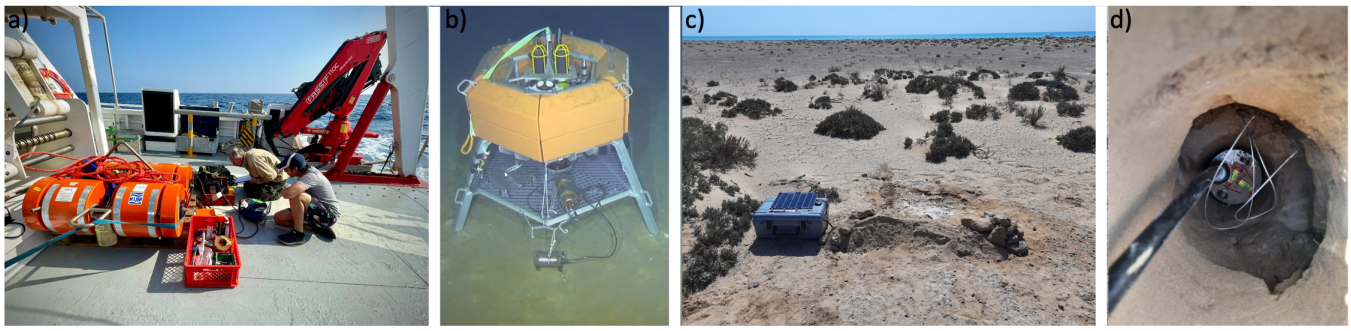

Figure 2 Photos of the seismic equipment used in the ZAFRAN network. a) A DEPAS OBS on the R/V Thuwal. b) Fugro multi-sensor lander with seismometer on the sea bottom. c) Installation of the island station BREEM (see Figure 1; setup identical to onshore stations). The grey box contains the data logger and the batteries. The solar panel and GNSS antenna are placed on the box. The seismometer is buried (not visible) and connected to the logger by the black cable. d) Example (in KHUF) of seismometer installation before filling the hole with sorted sand.

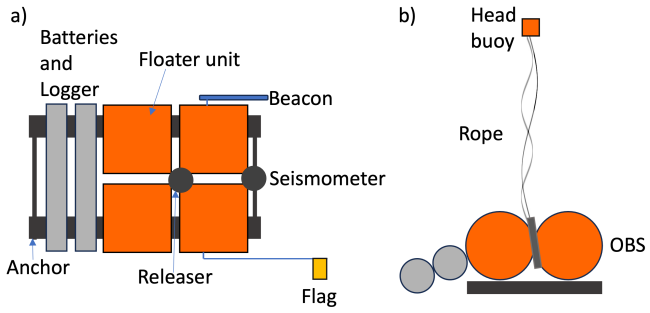

Figure 3 Schematic representation of the DEPAS OBS (Lobster)from a) above and b) from the side. Both sketches are not in scale. A head buoy is attached to the OBS with a free rope; half of the DEPAS OBS had the rope free to strum like in b) and the other half had the rope fixed on the anchor.

face. While 11 of the 12 DEPAS OBSs were successfully recovered during two trips in November 2022, communication with one of the OBSs (OBS04) was not successful, such that an additional trip was required in January 2023 when an automatic release had been scheduled. On 16 January 2023, the OBS04 was recovered without showing any damage, so the reason for the earlier unsuccessful recovery remains unknown. Skew values (difference between the time of the data logger and the instantaneous GNSS time) were measured for all DEPAS OBSs, except for OBS04, and are available in Suppl. Table 1.

Partially overlapping in time with our DEPAS OBS deployment, Fugro conducted an experimental deployment of two multi-sensor deep landers that include OBSs (Figure 2b). The Fugro OBSs were deployed in September 2021 from S/V Kobi Ruegg and visited in February and July 2022 with OSS Handin Tide. During the visits, the landers were fully recovered and redeployed after data collection and instrument maintenance. The OBS setup and deployment protocol for the Fugro OBSs were different from the DEPAS OBSs. After the landers reached the seafloor, an ROV was used to place a Nanometric Trillium Compact OBS 120s seismometer at the seafloor. It was enclosed on a light frame with feet to couple with the seafloor sediments. The seismometer was in an aluminum casing that weighs 2.9 kg in water. The data-logger Nanometric Pegasus OBS and batteries were on the lander and connected to the sensor with a cable.

During the visit in February 2022, the SOUTH data logger was found to have a minor leakage, and no data were recovered due to a damaged cable. The OBS from the lander NORTH was recovered and deployed on the lander SOUTH. Data from SOUTH were then finally recovered in July 2022. The skew values are not available.

Skew values for the Lobster OBSs range from 0.01 to 1.3 s, with a median of 0.37 s (Suppl. Table 1). The highest skew value was found for OBS08 that, together with the issues described in section 2.3, may indicate a possible general malfunction of the instrument. When excluding OBS08, the median (mean) skew value is 0.33 s (0.34 s). Although the skew values for OBS04 and NORTH are missing, these can be recovered using ambient noise cross-correlations between onshore and offshore stations (e.g., Naranjo et al., 2024).

We determined the orientation of the horizontal components of the off-shore seismometers using two distinct, data-type-based methods implemented in the open-source Python package (OrientPy; https://github.com/nfsi-canada/OrientPy). The first method is based on minimizing the P- and PP-wave energy on the transverse component (Braunmiller et al., 2020) while the second method is based on the arrival angle of minor- and major-arc intermediate-period surface-waves of teleseismic earthquakes by using modern global dispersion maps (Doran and Laske, 2017). For each station, we select the orientation according to the method with the smaller uncertainty (Suppl. Table 1). The method based on the polarization of surface waves yields smaller uncertainties for almost all the stations, except for OBS08 and OBS10. For benchmark and completeness, we also calculate the orientation of the onshore stations that resulted to be always lower than 10^o. The final median of uncertainties is 12.2^o.

2.2 Onshore deployment

We complemented the OBS network by installing four onshore stations. Two of them were located on the

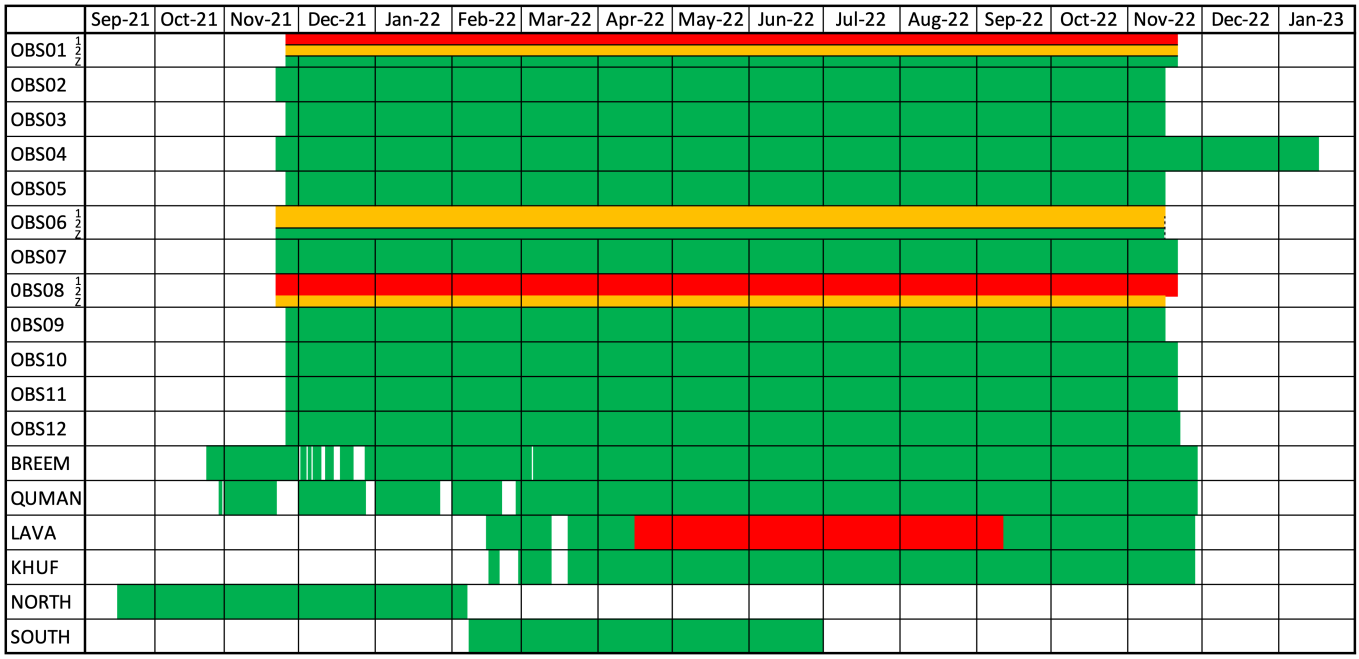

Figure 4 Data availability of the ZAFRAN dataset from September 2021 to January 2023. Green corresponds to waveforms available in three components. Yellow corresponds to data needing further preprocessing before being used. Red represents station or component failure. Note that there are three lines for each station, for the vertical (Z) and two horizontal (1 and 2) components.

small uninhabited reef islands Quman (3 km wide) and Breem (6 km wide) of the Al Wajh platform (Figure 1 and 2c). We refer to these stations as the "island stations". Station QUMAN is located within the Al Wajh lagoon whereas BREEM is located on the edge of the platform, making it more exposed to open sea environmental conditions.

The other two stations were installed onshore at a distance of 15 km (KHUF) and 25 km (LAVA) from the coast (Figure 1). Selecting locations closer to the coast was not possible because of coastguard permit limitations and lack of solid bedrock. We refer to KHUF and LAVA as the "land stations" and to both the island and land stations as the "onshore stations".

The island stations were equipped with Nanometrics Trillium Compact Horizon sensors and the two land stations with Nanometrics Trillium Compact posthole sensors. Both types of sensors have a flat response of up to 120 s and can be used in direct burial installations. The sensors were buried within a depth of 50 cm in a cylindrical hole that was 2 cm larger in diameter than the sensor (Figure 2d). The bottom of the hole was filled with a thin layer of sorted fine sand to easily level the sensor. The little space remaining between the hole and the sensor was filled with the same sand providing coupling and thermal insulation. The two island sensors were deployed within porous, but hard, coral rocks, and the two land sensors were installed within the Precambrian bedrock.

The onshore stations were equipped with Nanometrics Centaur dataloggers powered by lithium batteries charged by a 30 x 40 cm solar panel (Figure 2c). Sand accumulation on solar panels is a well-known issue, especially in this part of the world, and since a definitive solution has not been found yet, data recording has suffered a few gaps because of power issues. Stations were visited for maintenance, and data were collected every 3-6 months.

2.3 The collected dataset

The ZAFRAN dataset includes about 12 months of data from the DEPAS OBSs, 5 months from the Fugro OBSs, 14 months from the island stations, and 10 months from the land stations (Figure 4). More specifically, we collected data for 358 overlapping days with the 12 DEPAS OBS. OBS04 recorded 57 days more than the other DEPAS OBSs. While all the instruments were equipped with 3-component sensors, the quality of the horizontal component 1 of OBS01 and both horizontal components of OBS08 is poor and cannot be used for seismological investigations.

In addition, the vertical component of OBS08 can only be used for half of the recording days (this issue is discussed further in section 3.1). Even considering these data losses, the recovery rate for the DEPAS OBSs is over 90%.

The data of OBS NORTH complements the ZAFRAN dataset with 140 days that overlap for 73 days with the DEPAS dataset. Data from OBS SOUTH span 144 days and completely overlaps with the DEPAS dataset. Considering the initial plan (see section 2.1), the Fugro OBSs had a recovery rate of 50%. Furthermore, the two island stations recorded about 330 days of data, each with an average recovery rate of 96%, and fully overlapping with the DEPAS dataset. Finally, the two land stations provided 270 (KHUF) and 140 days (LAVA) of data at a recovery rate of 95% (KHUF) and 49% (LAVA).

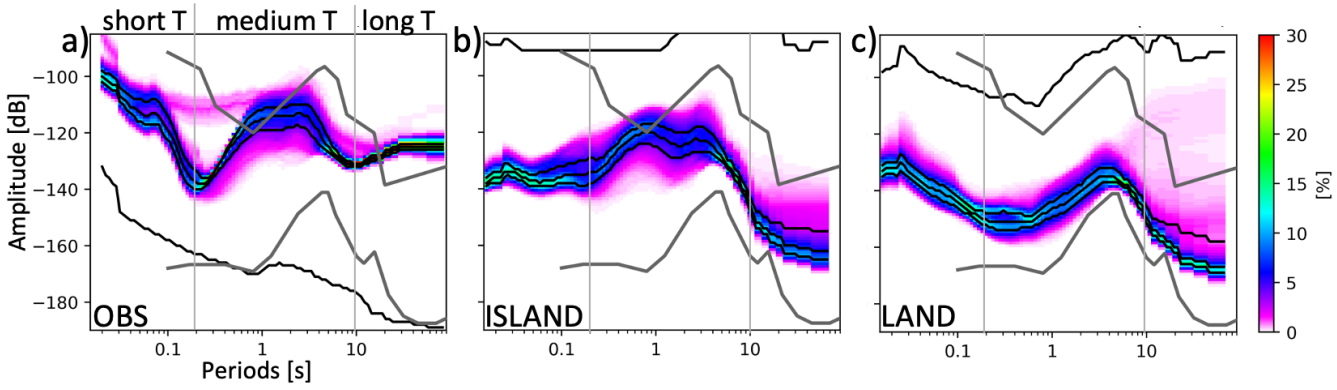

Figure 5 Examples of Probabilistic Power Spectral Densities (PPSD). a) PPSD of the Z component of the station OBS10 calculated for all available data. b) Same as for a) but for the island station BREEM. c) As for a) but for the land station KHUF. Dark gray curves represent the New High Noise Level and the New Low Noise levels (McNamara and Buland, 2004). Black lines correspond to the 25th, 50th (noise level), 75th and 100th. Light gray vertical lines represent the boundaries separating ranges of short, medium, and long periods (T).

3 Noise levels

Noise levels serve as valuable indicators for assessing station performance across different components and for investigating the sources of ambient seismic noise recorded at specific stations. While it is not always straightforward to distinguish the impact of a station's low performance from that of a strong noise source, we discuss the characteristics of noise levels that are primarily associated with instrument type and installation in Section 3.1, and we conduct a preliminary analysis of the noise sources (Section 3.2) to distinguish them from potential issues related to station performances.

To accomplish this, we calculate the Probabilistic Power Spectral Densities (PPSD McNamara and Buland, 2004) as implemented in ObsPy (Beyreuther et al., 2010) for all available data using time windows as small as 450 s and an overlap of 50 %. Examples of PPSD for an OBS, an island, and a land station are shown in Figure 5. We refer to noise level as the median of the PPSD for a given time window (see Figure 5). If not specified, we refer to the entire deployment period of a given instrument.

In our analyses, we divide the overall period range into three segments: short-period ($T < 0.2$ s), medium-period ($0.2 \leq T \leq 10$ s), and long-period ($T > 10$ s). We select the boundaries of 0.2 and 10 seconds due to their alignment with the two predominant notches observed in the PPSD of the ZAFRAN network (see gray vertical lines in the plots of Figure 5). All noise levels are shown in Figure 6 where stations are grouped in classes, depending on the shape of the noise level in the medium-period range. These classes are further discussed in Section 3.2.2.

3.1 Station performances

The two onshore stations, KHUF and LAVA, exhibit the best data quality within the ZAFRAN network, characterized by consistently low noise levels (Figure 6a-c). Their exceptional performance can be attributed to their good subsurface coupling, effective insulation, and remote locations (far from anthropogenic noise sources). However, LAVA displays elevated long-period noise across all components compared to KHUF. This discrepancy may be attributed to thermal insulation limitations, which are also responsible for sensor failures due to high temperatures (see Section 2.2).

The performance of the two island stations, BREEM and QUMAN (Figures 6d-f) is similar to the two land stations because they share the same instruments and style of installation. However, QUMAN exhibits an unusual peak at approximately 4-6 Hz. A visual inspection of waveforms and spectrograms reveals consistent, high-amplitude noise between 10 Hz and 0.8 s, most likely due to construction activities at Red Sea Global. This aspect needs to be considered when using the data for local seismicity studies.

All ZAFRAN stations exhibit a noise level notch between 9 and 11 s (Figure 6). Beyond this period, noise levels consistently increase for nearly all DEPAS OBSs in all components. In contrast, Fugro OBSs maintain low long-period noise in the vertical component, comparable to onshore stations. However, the horizontal components of Fugro OBSs exhibit high noise levels, similar to DEPAS OBSs. These results are in agreement with Stähler et al. (2018) who compared the noise recorded by seismometers deployed inland and offshore to test the Lobster OBSs of the DEPAS pool managed by the Alfred-Wegener Institute. The authors analyzed the noise recorded by the Güralp CMG-40T seismic sensor in vault conditions and the Güralp CMG-40T-OBS at sea. This CMG-40T-OBS is the same sensor but modified to be included in the OBS. They found that the self-noise of the CMG-40T-OBS is higher than the noise produced by the corresponding original model at wave periods larger than 10 s. Their tests also demonstrated that the DEPAS OBSs perform better at longer periods if a Nanometrics Trillium compact seismometer substitutes the CMG-40T-OBS.

Fugro outperforms DEPAS OBSs in the short-period range, likely due to the fewer additional elements on the OBSs that could resonate with marine currents, as discussed in previous studies (Stähler et al., 2016; Essing

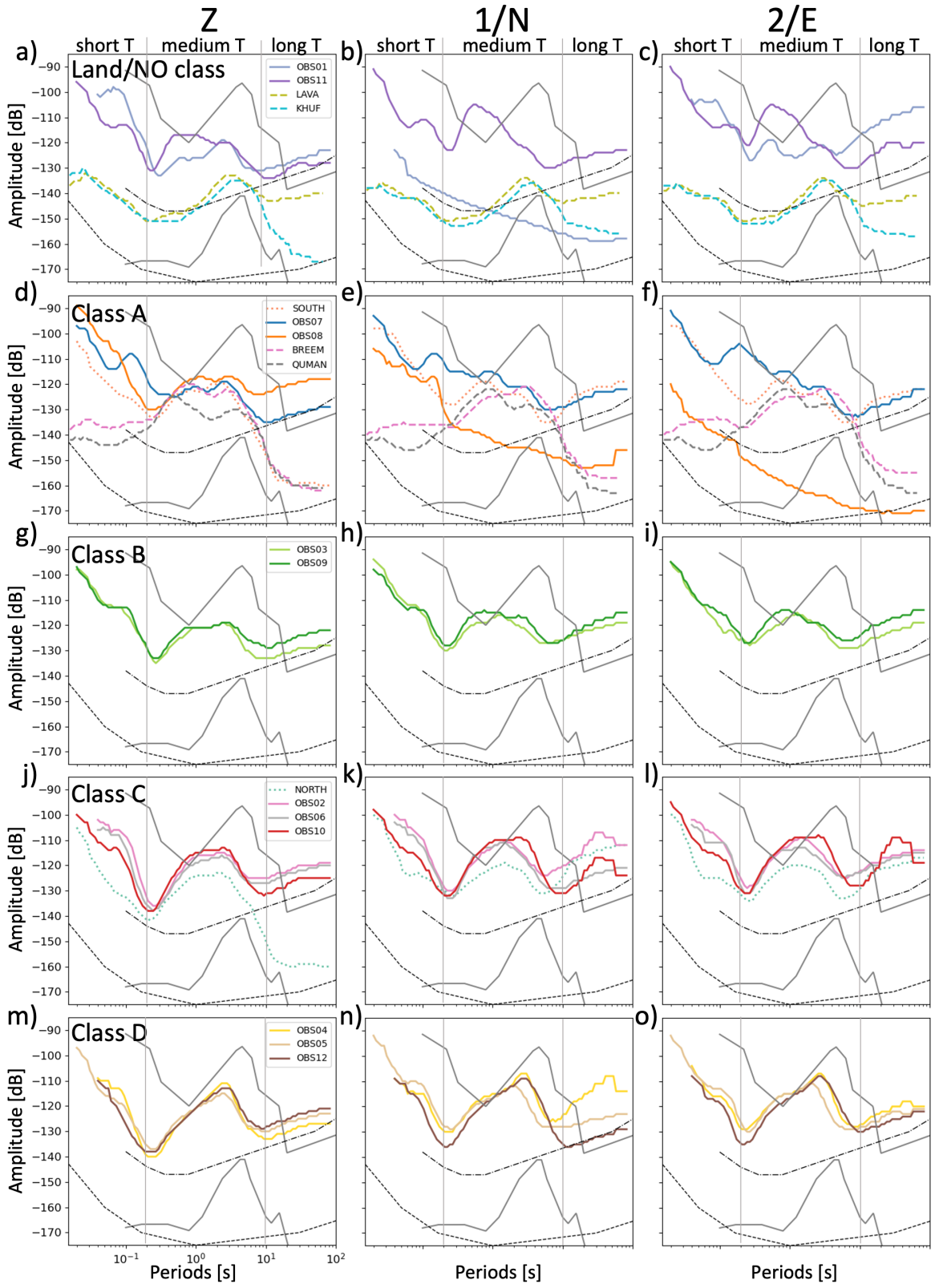

Figure 6 Noise levels (median of PPSD) for the ZAFRAN dataset grouped by similarity in the medium-period range. a) Noise levels for the land stations and two OBS that have unique noise levels for stations of class A and vertical components. b) As in a) but for 1/N components. c) As in A but for Z/E components. d), e) and f) As in a), b) and c) but for the stations in class A. g), h) and i) As in a), b) and c) but for the stations in class B. j), k) and l) As in a), b) and c) but for the stations in class C. m), n) and o) As in a), b) and c) but for the stations in class D. Colored dotted, solid, and dashed lines represent the noise levels of the Fugro OBSs, DEPAS OBSs, and onshore stations, respectively. Noise levels of LAVA do not include days of sensor failure. Gray lines represent the New Low Noise Model and New High Noise Model, respectively (Peterson, 1993). Black lines represent the self-noise of the CMG-40T-OBS (dot-dashed, Stähler et al., 2018) and the Trillium compact (dashed, from the manufacturer).

et al., 2021a; Corela et al., 2022).

However, as already observed by Janiszewski et al. (2022) and valid in our deployment, it is not trivial to separate the effects due to the type of seismometers from the overall OBS setup in the noise level. This also applies to our deployment of two OBS setups with two different sensor types.

An overview of signals recorded by the ZAFRAN network, given in terms of spectrograms calculated from the PPSD (Figure 7), offers further insights into the data quality. The most prominent signal across all stations is the microseisms in the medium-period range (see example in the red "MS" box of Figure 7). Additionally, teleseismic events are visible at several stations in the medium and long-period ranges (see an example within the red box "TL" in March 2022 in Figure 7). Furthermore, local earthquakes are visible in the short-period range (see an example red box "LOC" on 30 June 2022 in Figure 7). These distinct and clear signals serve as evidence of the high-quality nature of the ZAFRAN dataset.

The analysis of noise levels and 1-year spectrograms also highlight sensor failures. The noise levels of the horizontal components 1 of OBS01 and 1 and 2 of OBS08 show that these seismometers' components most of the time did not record properly (Figure 6b and 6e-f). The OBS08 spectrogram (Figure 7) illustrates that the sensor malfunctioned also in the vertical component for approximately 40% of the installation duration. Similarly, the sensor at station LAVA experienced a failure from mid-April to mid-September (Figure 7), likely due to elevated air temperatures (see Section 2.2). Lastly, when examining spectrograms for onshore stations (LAVA, KHUF, BREEM, and QUMAN in Figure 7), we observe intermittent data gaps, which we suspect to be due to sand accumulation on the solar panels. The overall usability of the dataset is summarized in Figure 4.

3.2 Environmental and geological noise sources

Noise levels can also provide insights into environmental (ocean and atmosphere) and geological (subsurface) factors. In this section, we present a preliminary analysis of potential noise sources in the short, medium, and long-period ranges that can be used as a reference for future studies based on the ZAFRAN dataset.

3.2.1 Short-period ranges

Sources of short-period ($\leq$ 0.2 s or $\geq$ 0.5 Hz) noise can be geological (e.g., local earthquakes, volcanic tremors, etc.) or due to the interaction of sea-bottom currents with the structural components of the OBS (Corela et al., 2022). In addition, noise due to passing ships and marine mammals must be considered.

In general, the short-period noise levels of the ZAFRAN deployment are overall high when compared to PPSDs published from previous experiments in the oceans and lakes (e.g., Stähler et al., 2016, 2018; Hilmo and Wilcock, 2020; Carchedi et al., 2022; Kim et al., 2023; Zhang et al., 2023). For example, ZAFRAN noise levels from the OBSs on the vertical component are in the range between -125 and -110 dB (Figure 6). Most of the noise levels recorded in the Indian Ocean by using the DEPAS OBS (Stähler et al., 2016) and in the South Atlantic (Zhang et al., 2023) are about -130 dB in the same component and frequency. Off the coast of the Pacific Northwest, the noise is between -160 and -150 dB (Hilmo and Wilcock, 2020). The same range of values is found in western Pacific (Kim et al., 2023). In the Malawi Lake, values are about -150 dB (Carchedi et al., 2022). Instead, our short-period noise levels are similar to the noise recorded in shallow water (22 m) of the Baltic Sea (Stähler et al., 2018).

To better understand the origin of the high short-period noise and to identify potential geographical noise patterns within the ZFZ, we plot the noise levels averaged within the short-period range for the vertical and the average of the two horizontal components (Figure 8a and 8e). The geographical noise distribution in the short-period range defines different domains and subdomains. The southern and central offshore domains (labeled "SO" and "CO" in Figures 8a and 8e) reveal higher short-period noise than the northern offshore ("NO") domain for both vertical and horizontal components (Figures 8a and 8e). The limit between these two domains corresponds to the Mabahiss deep (see Figure 1) and the commonly used limit between the central and the northern Red Sea. Finally, for the CO domain, we notice an increase in noise from the island stations offshore for the vertical component. Global maps depicting ship route density (from marinetraffic.com, last access Dec 13, 2023) reveal that the Red Sea is among the most traversed routes, with common shipping routes situated closer to our deployment south of Mabahiss and gradually moving farther north. This fact suggests that ship traffic may contribute to the elevated noise levels and its variation towards the north and offshore.

Another interesting feature of the short-period noise at almost all OBS is a peak at around 0.1 s (10 Hz, Figure 6). Exceptions are OBS05, OBS08 and OBS12. This could be due to a poor coupling between the seismometer and the anchor or between the anchor and the seafloor. However, the reasons for the presence or absence of this peak remain unclear.

Next, we analyze the correlation between noise levels and water depth for the vertical components and for the average of the two horizontal components (ρ^{V}_{depth} and ρ^{H}_{depth}, respectively; see Figures 8d and 8h). We group the stations by OBS setup (Fugro and/or DEPAS and loose/tight rope) and we consider only correlation coefficients larger than 0.5. For the short-period noise levels, we find a positive correlation for the horizontal components of the DEPAS OBSs with loose rope (ρ^{H}_{depth}=0.73) suggesting that the rope may act as a resonant noise-generating element, possibly due to sea-bottom currents. However, given the limited number of stations, this correlation of noise with water depth may not be robust.

Regarding temporal variations of short-period noise levels, all stations exhibit similar patterns across all components. For most stations, the noise remains stable or gradually decreases during the deployment, typically not exceeding a 10 dB change (Figure 9), probably

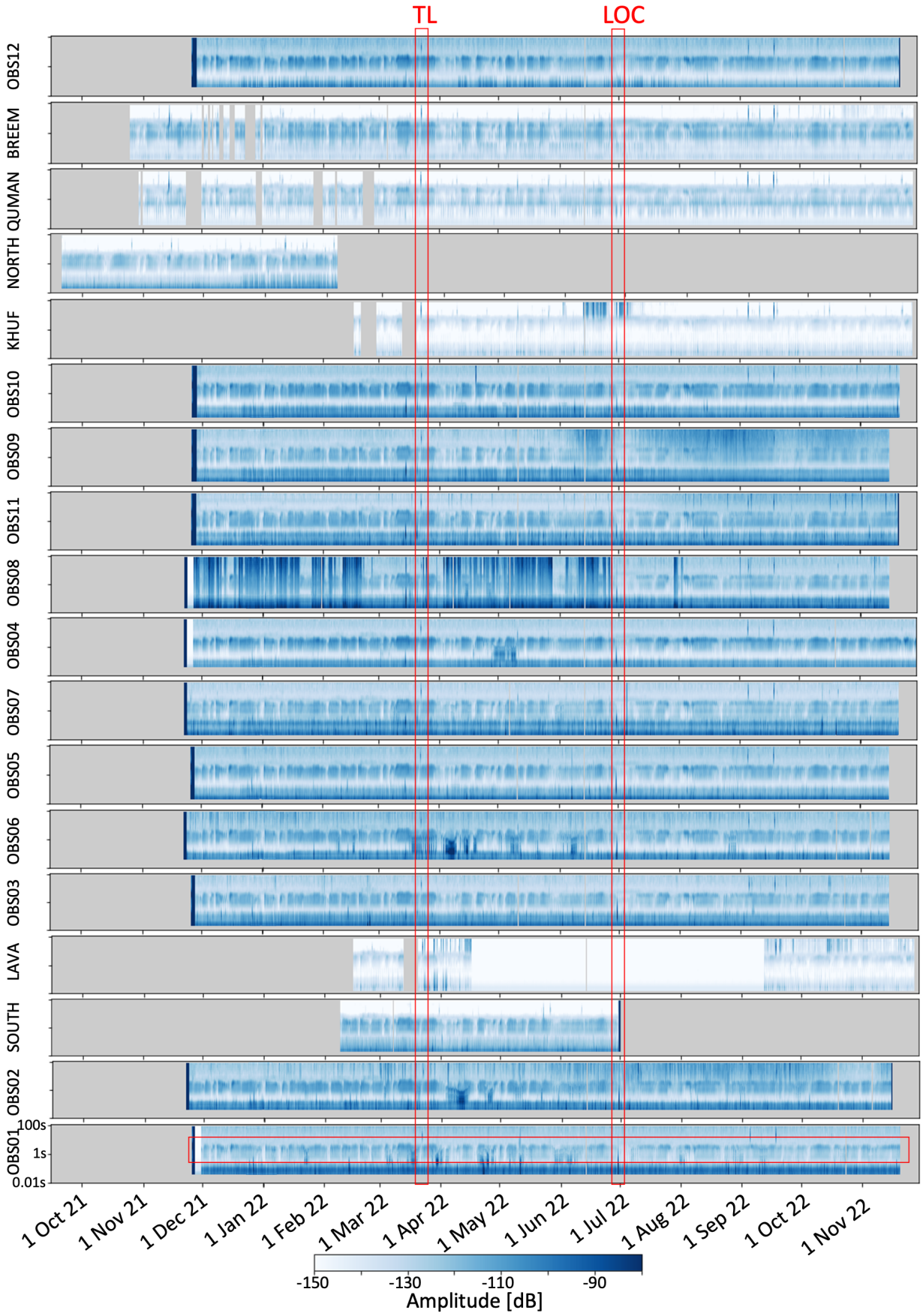

Figure 7 Deployment overview in terms of spectrograms, showing the temporal variations of the PPSD for the vertical component of each station. The vertical scale of each spectrogram is as in the bottom one. Stations are ordered from South (bottom) to North (top).TL: example of teleseismic earthquake. LOC: example of a local earthquake. MS: example of microseismic noise.

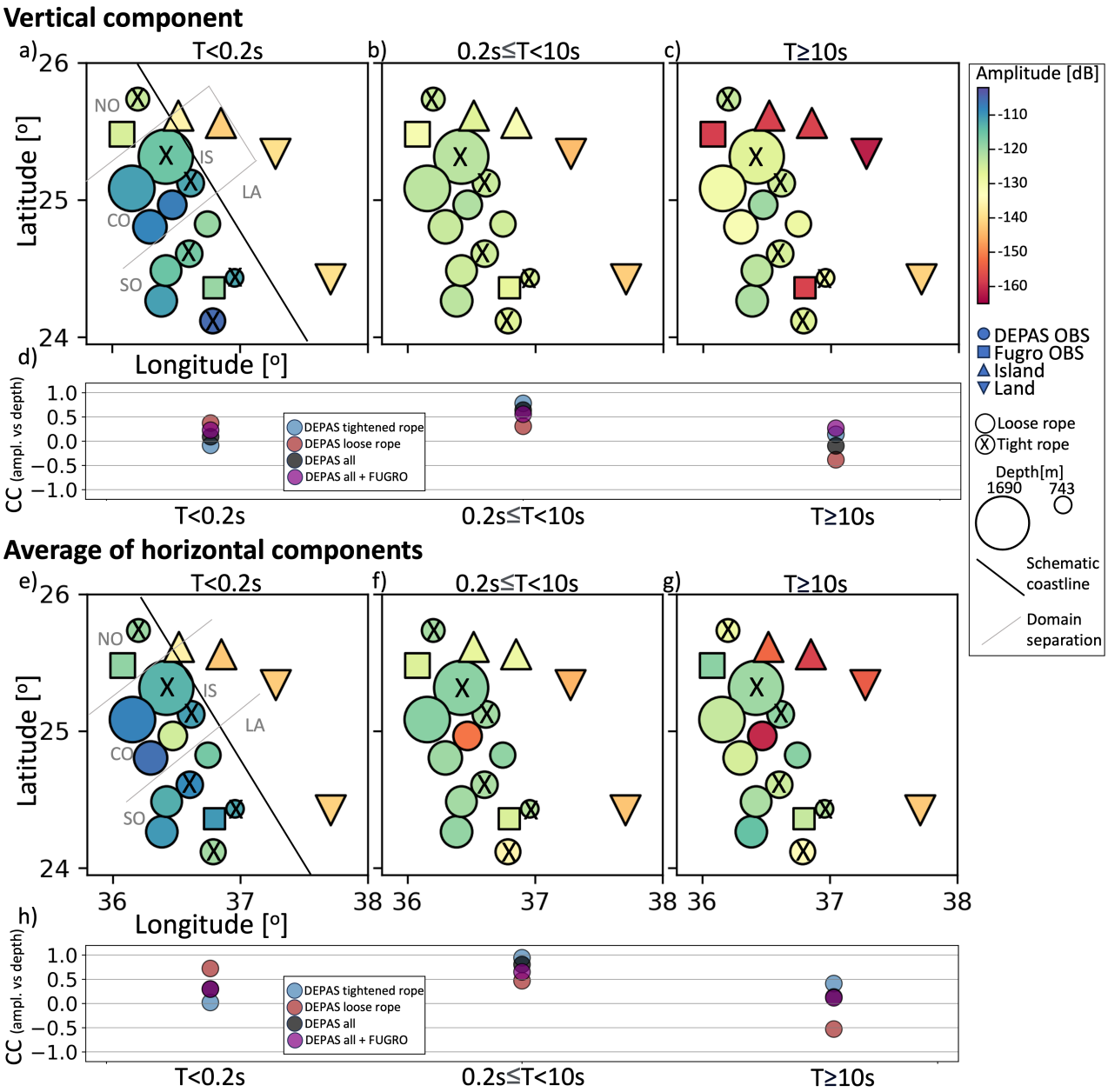

Figure 8 Spatial variations of noise levels. a) Average noise levels for the vertical components at period $T < 2\,s$. NO: northern offshore; CO: central offshore; SO: southern offshore: IS: island/lagoon; LA: land. OBS markers are scaled by water depth. b) and c) as for a) but for periods 0.2 - 10 s and ≥10 s, respectively. d) Correlation coefficients between the noise levels on the vertical components and water depth. e), f) and g) as for a), b) and c), respectively, but for the horizontal components. g) As for d) but for the horizontal components.

due to the settling of the instruments on the seafloor becoming more stable. One exception is QUMAN, where short-period noise increases during deployment, likely due to the anthropogenic noise (see section 3.1). Another exception is NORTH, which shows a sharp noise increase of approximately 10 dB from December 2021 to January 2022. Given that NORTH is located on Mabahiss Mons, whose volcanic activity is unknown, it is challenging to determine whether this increase results from changes in volcanic activity, instrument issues, or another unknown phenomenon.

3.2.2 Medium-period range

The secondary microseismic peak is visible on all ZAFRAN stations typically between 1 and 4 s (0.25 - 1 Hz). The island stations and most OBSs also exhibit a second peak at periods between 0.2 and 1 s (1 and 5 Hz, Figure 6). However, this peak is not visible at the land stations (see comparison in Figure 5) and at OBS04, OBS05, and OBS12 (Figure 6m-o). To better understand these differences, we visually classify stations based on the shape of their noise level patterns in the medium-period range, primarily related to the presence or absence of the second peak and the degree of overlap between the two peaks.

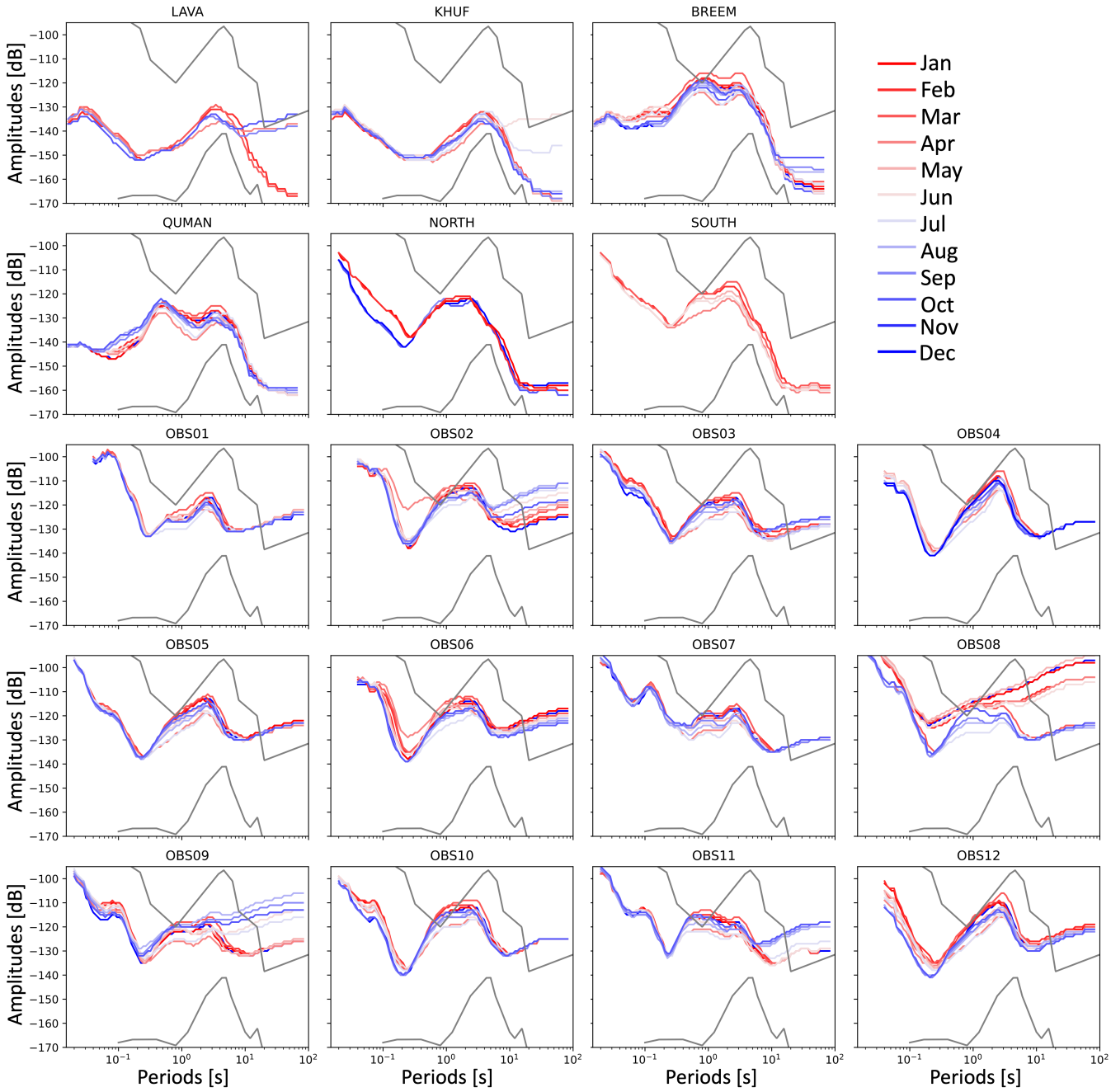

Figure 9 Temporal (monthly) variations of noise levels. Noise levels of the vertical component of all ZAFRAN stations are calculated in monthly time windows. Gray lines represent the New Low Noise Model and New High Noise Model, respectively (Peterson, 1993).

Class A includes stations with two well-separated peaks, such as the island stations QUMAN and BREEM, the Fugro OBS SOUTH, and DEPAS OBS OBS07 and OBS08 (Figure 6d-f). Stations with slightly separated peaks, like OBS03 and OBS09, fall into class B (Figure 6g-i). Class C encompasses stations with noise levels displaying a single large peak rather than two separate peaks (Figure 6j-l), including NORTH, OBS02, OBS06, and OBS10. OBS04, OBS05, and OBS12, which lack a visible second peak, are classified as class D. OBS01 and OBS11 did not fit into any of the predefined classes (Figure 6a-c). Notably, we could not identify any correlations between classes and water depth, geographical location, or instrument type/setup.

To investigate potential correlations between the seismic noise and oceanographic and meteorological phenomena, we use two ERA5 datasets from ECMWF (European Centre for Medium-Range Weather Forecasts, Hersbach et al., 2023, last access 29 August 2023). These ERA5 datasets are reanalyses, consisting of hourly time series and combining models with observational data. Specifically, we examined the 10-meter vertical wind component (10v) with a spatial resolution of 0.25°, representing northward wind at a height of 10 meters, and the significant wave height (swh), which combines wind waves and swell, also at a resolution of 0.25°. We use the Pearson coefficient to estimate the level of correlation between the time series of the noise, hourly resampled,

and the time series of 10v and swh.

In our analysis, we use two weeks of data (1-14 January 2023 or 1-14 April 2023, depending on the availability) from the DEPAS OBS12, the Fugro OBS NORTH, the two island stations (BREEM and QUMAN), and the land station KHUF and we compare them with 10-meter vertical wind component (10v) and the significant wave height (swh, only used for OBSs data analysis) for the same time windows. Figure 10a shows an example of time-series comparisons for the noise levels of the OBS12 at 0.7 s, 10v and swh at the same location. After calculating the Pearson coefficients for the two parameters (ρ_{10v} and ρ_{swh}) for the full period range, we observe that both curves ρ_{10v} and ρ_{swh} exceed 0.75 in the medium-period range (Figure 10b-c) and are low outside the medium-period range. Also, while the maximum correlation is higher for swh, both correlation curves exhibit a double peak. For both OBSs, the correlation with swh peaked at 1 and 3 s, while the correlation with 10v peaked at 0.5 and 2 s. The periods of the two peaks in the correlation curves align with the periods of the two peaks of the noise levels in the medium-period range observed in most of the ZAFRAN stations. Interestingly, it is worth noting that even though OBS12 belongs to class D (no second peak), ρ_{10v} and ρ_{swh} still exhibit the double peak. For the island stations, ρ_{10v} is slightly lower than that for the OBS. Although the two peaks in the correlation curve are less pronounced, the overall curve shape is similar (Figure 10d-e). For the land station, ρ_{10v} is less than 0.25 but two peaks and the overall shape of the curve are preserved (Figure 10f).

Time-series environmental correlations between noise levels and wind speeds (e.g., Bromirski et al., 2005; Hilmo and Wilcock, 2020) and significant wave height (Zhang et al., 2023; Kim et al., 2023) were already present in literature. Our analysis adds insight on the atmosphere-ocean-Earth interaction clearly showing the frequency domain of influence on the medium-period range noise of these two environmental factors, that for the Red Sea is between 0.2 and 10 s.

Maps in Figures 8b and 8f show small noise variations within the medium-period range with some increase of the noise noticeable going from land stations (LA) to the inner lagoon (easternmost station in IS) to the external lagoon (westernmost station in IS) to offshore.

Regarding the correlation between the noise levels and water depth at the medium-period range, ρ_{depth} is larger than 0.5 for all groups and components considered, except for the DEPAS OBSs with a loose rope. Considering the correlation found between the noise level and the 10v and swh, it is surprising that the noise may increase with water depth. As for the short-period range, these correlations may not be robust enough.

The monthly noise variations at medium-period range across the components are similar for most of the stations, with differences of less than 15 dB between the noisiest and quietest months (Figure 9). During the summer months of the northern hemisphere, typically May, June, and July, we observe a decrease in noise levels (Figure 9). OBS01, OBS02, and OBS06 stand out because noise reduction occurs primarily in July. Interestingly, while the amplitudes vary in time, the presence or absence of the double peak does not (no change of class in time).

3.2.3 Long-period range

To understand the contribution of the sea bottom currents and tilt on the long-period noise, we use the coherence between the vertical and the two horizontal components calculated by using a modified version of the open-source OBS tools code (Janiszewski et al., 2019) that implements the method of Crawford and Webb (2000). Specifically, we calculate daily coherence as a function of the periods for each OBS for the whole duration of the deployment and consider the median coherence (analogously to the noise levels) between the vertical component of each station and the two horizontal components. Finally, we calculate the mean value for periods > 10 s. We observe a very low coherence for both DEPAS OBS (average between stations and component is 0.07) and Fugro OBSs (average is 0.1). While the low coherence agrees with the low noise levels in the vertical components of Fugro OBSs, the high noise in their horizontal components likely results from sea bottom currents. These instruments can automatically level, regardless of initial tilt, preventing horizontal noise from affecting the vertical component. Conversely, the high noise levels in both the vertical and horizontal components of DEPAS OBSs, coupled with low coherence, are probably due to the high self-noise.

We observe that one or both horizontal components of the OBS02 and OBS10 (Figures 6b-c) show a peak between 20 and 50 s. This is a stable feature for the duration of the deployment but for which we currently have no explanation. KHUF, BREEM, and QUMAN are the only stations with a weak primary microseism peak (10-12 s) visible on the vertical components, probably since the high self-noise at periods larger than 10 s is higher than the typical average amplitudes of the primary microseismic peak at the offshore stations.

The observed long-period noise patterns in Figures 8c and 8g suggest that nearby stations tend to have similar noise levels on both vertical and horizontal components. For instance, OBS06 and OBS02, two closely located stations, exhibit the highest noise levels in the vertical component.

Lastly, the most notable feature from the maps in Figures 8c and 8g is the correlation with the instrument types discussed above with the Fugro OBS having systematically lower noise than DEPAS OBS in the horizontal components, and with the onshore stations performing systematically better than offshore stations.

In the long-period range, the only strong correlation between noise and water depth is ρ^{H}_{depth}=-0.56 for the DEPAS OBSs with the free rope, as already seen for the short-period range (Figure 10f and 10j). The negative correlation between noise and water depth aligns with findings in previous studies (e.g., Janiszewski et al., 2022).

Long-period noise levels remain relatively stable with time for most stations (Figure 9). OBS09 and OBS11 experienced sudden increases of 15-20 dB after the summer period, while OBS06 and OBS12 gradually de-

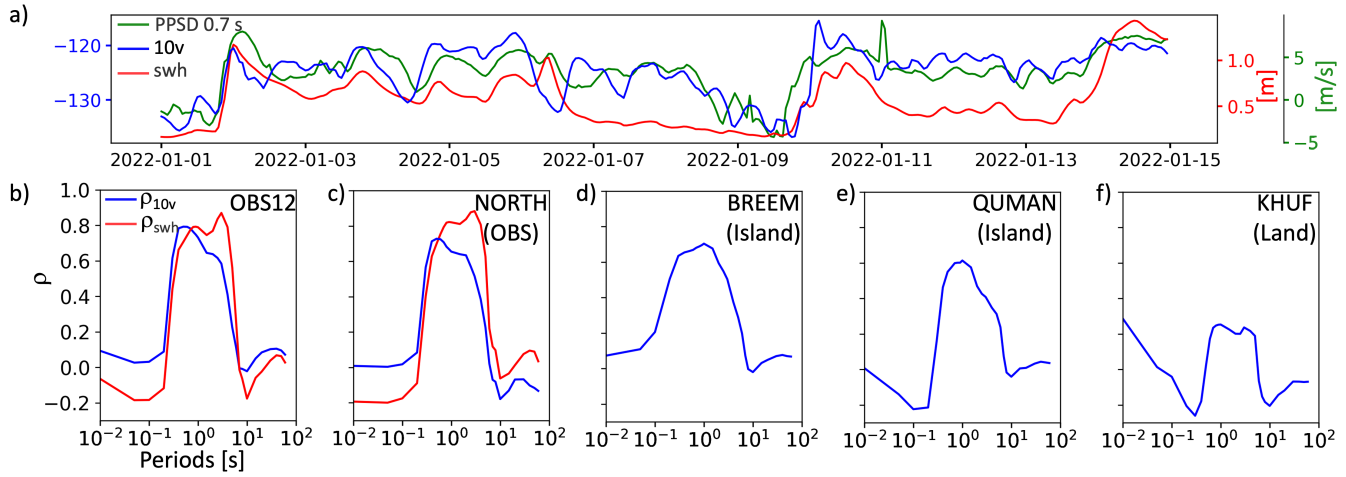

Figure 10 Correlation between environmental data and noise levels. a) Example of comparison of 14-week-long (1-14 January 2022) time series of vertical-component noise levels at the period of 0.7 s for OBS12 against 10-meter vertical wind component anomaly (10v) and significant height of combined wind waves and swell (swh) at the OBS12 location. b) Variation of the Pearson coefficient between noise levels at Fugro OBS NORTH and 10v and swh with the noise level. c) As in b) for DEPAS OBS12. d) As in a) but for island station BREEM (only 10v data available). e) As for d but for island station QUMAN. f) As for d) but for land station KHUF.

creased in noise levels during the deployment, possibly due to instrument settling. OBS02, on the other hand, exhibited a 15-20 dB increase during the summer months, followed by a return to initial values.

4 Notable signals

In this section, we present and briefly discuss some notable seismic signals found in the ZAFRAN dataset that are partly related to the specific setting of the Red Sea and partly due to the deployment and instruments used.

4.1 Long-lasting high-frequency tremor

A notable signal observed within the ZAFRAN network is a recurring, several-hour-long tremor in the 0.025 - 0.25 s period range (4 - 40 Hz). To show this, we plot several one-day spectrograms of the 1/N components for some OBSs and onshore (island and land) stations (Figure 11). We highlight this long-lasting high-frequency tremor by using a dotted-line box on the spectrogram where it is most visible (OBS12). Nonetheless, this signal displays strong amplitudes in the majority of stations, whether offshore or onshore, with the exceptions being QUMAN (the island station), LAVA (the land station), and OBS11. In the spectrograms in Figure 11, this signal starts at around 3 h and it continues for the rest of the day. Although systematic detection has not been conducted as of yet, this type of event is frequently observed in the ZAFRAN datasets, occurring at different times and enduring for several hours. Since the waveforms for these events do not show a sharp onset, their localization is not trivial and is not performed at this stage.

Potential sources of these signals are anthropogenic, such as due to the passage of ships, active seismic surveys, or may originate from various factories (e.g., desalination, refining, cement production) situated along the coast of the study area, particularly in the areas of Al Wajh, Umm Luj, and Yanbu (Hamieh et al., 2022) (see locations in Figure 1). If this is the case, the higher amplitudes observed at the offshore stations might be attributed to more efficient energy propagation over water, possibly facilitated by T-waves traveling through the ocean sound channel (Heleno et al., 2006). Nonetheless, we cannot rule out the possibility of a natural origin (e.g., volcanic tremor from Mabahiss Mons). Heleno et al. (2006) observed tremors with comparable characteristics (duration, frequency, and propagation efficiency) in the Cape Verde islands and proposed active seamounts as potential sources.

4.2 Free rope signature

As described in Section 2.1, half of the DEPAS OBSs were deployed by tightening the rope of the buoy (avoiding free strumming in the water column), and the other half was deployed leaving the rope free to strum on the water column above the OBS (see Suppl. Table 1) and a sketch of the OBSs with free rope in Figure 3b). One-day-long spectrograms of OBSs with the free rope (Figure 11, right column) show two types of noise features that are not visible in the spectrograms of the stations with the tightened rope.

The first type of noise is visible only on the spectrograms of the stations with the free rope is recorded at frequencies above 5 Hz (0.2 s, the most evident example is highlighted in the dashed-dotted line box on the spectrogram of the DEPAS OBS02 in Figure 11). It is characterized by stronger amplitudes at specific frequencies and energy bursts of short duration repeated in time. All DEPAS OBSs with the free rope show this type of noise with some differences in the maximum amplitudes. While this disturbance was investigated by Stähler et al. (2018); Essing et al. (2021b); Corela et al. (2022) and identified between 1 and 10 Hz (0.1 and 1 s) here we

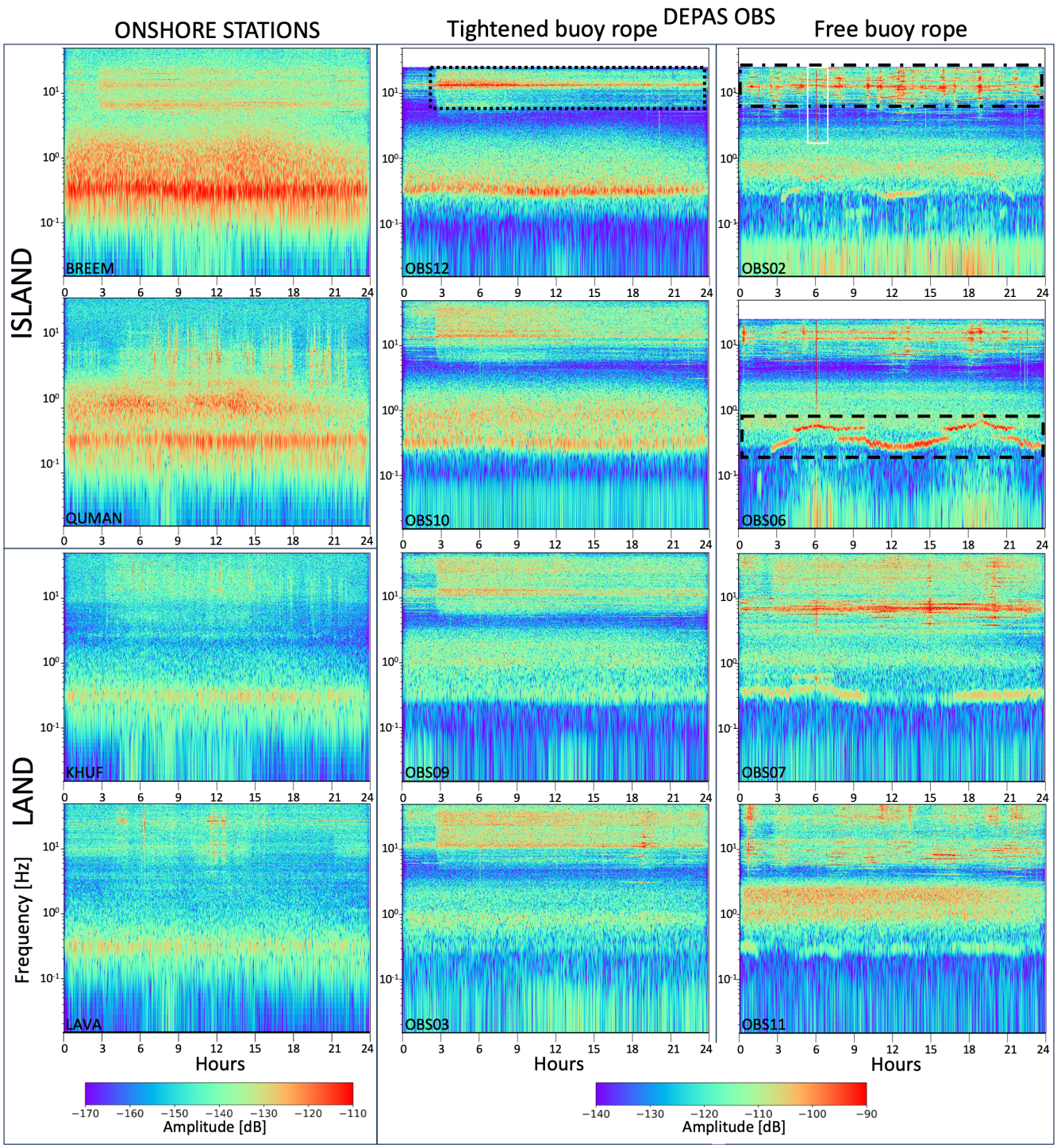

Figure 11 One-day spectrograms with examples of the notable signals detected by the ZAFRAN network. The left column shows the spectrograms for onshore stations (island stations in the first two rows and land stations in the last two rows). The central and right columns show the spectrograms for 8 of the DEPAS OBS. The central column contains spectrograms for OBS with tightened buoy rope. The right column contains spectrograms for OBS with a buoy rope free to strum in the water column. The dashed-line box on the spectrogram of OBS12 highlights an hours-long high-frequency signal (also evident in BREEM, KHUF, OBS10, OBS09, OBS03, OBS07). The dot-dashed-line box on the spectrogram of OBS02 highlights the high-frequency noise generated by the rope free to strum (also evident in all the other OBS with the free rope). The white box on the spectrogram of OBS02 highlights an example of a local earthquake (also visible in the spectrogram of OBS06). The dashed-line box on the spectrogram of OBS06 highlights a long-period tide-modulated signal (evident also in the other free buoy rope OBS). All spectrograms are calculated instrument-corrected acceleration waveforms of the horizontal component 1/N for March 1, 2022.

find that the free rope affects the dataset at frequencies higher than 5 Hz (0.2 s).

The second type of noise, visible only on the spectrograms of stations with the free rope, is a bi-daily tidal modulated signal with periods of 2-7 s. OBS06 exhibits the highest amplitudes of this signal (see the signal enclosed in the dashed-line box in Figure 11). Schlindwein et al. (2018) and Hannemann et al. (2016) found a similar signal in less than half of the DEPAS OBSs used in their deployments and as they could not identify the source, they assumed it to be of instrumental origin.

4.3 Hybrid local earthquake

We conduct a preliminary analysis of a local earthquake visually detected in the spectrograms of Figure 7 (see red box "LOC") that occurred on June 30, 2022. A 150s-long time window, containing this earthquake, is shown in Figure 12a. After manually picking P and S arrivals, we calculated the epicenter using HypoInverse code (Klein, 2002). The hypocentral depth is kept fixed at 5 km because it strongly depends on the velocity model, which still needs to be optimized for the ZFZ. Our preliminary calculations for earthquake location and magnitude suggest that this event occurred in the southern part of the network (see location indicated by the yellow circle in Figure 1) with a magnitude of M_L 3.4. This is likely the strongest local earthquake recorded by the ZAFRAN network since no stronger signals are seen in Figure 7 at high frequency. Not having access to the recent Saudi national catalog and being too small to be detected by the global networks, we cannot benchmark our location and magnitude estimate.

Qualitative waveform differences between stations may already reveal important information for future works. For example, waveforms (highpass filtered at 0.1 Hz) recorded by OBS10, KHUF, and OBS12 (Figure 12a) have smaller amplitudes after the P arrivals compared to waveforms in the other stations, probably due to weaker scattering effects. One hypothesis is that these differences are related to the site effects and that OBSs displaying waveforms with less scattering effects are located on thinner or no sedimentary cover (evaporites and/or loose sediments). Although the actual distribution and thickness of these sedimentary materials is not known in the ZFZ, this is consistent with the locations of OBS10, located in the deepest part of the ZFZ where the salt coverages seem to be limited, and OBS12, located on the flanks of Mabahiss Mons (Fittipaldi et al., 2024). While these site-effects may limit the ability to accurately pick the onset of the body waves both for location and focal mechanism calculations, they could be used for retrieving the shallow earth structure.

Waveforms for the same earthquake show a clear T-Phase at some of the stations (see boxes on waveforms of OBS04, OBS07, OBS09 OBS11, BREEM, and OBS12 in Figure 12a). T-phases are generated by the seismic-acoustic conversion and travel along the minimum sound velocity layer in the ocean (e.g., Okal, 2008). In our waveforms, the T-phase starts to be visible at stations farther than 70 km from the source (for closer stations, it is probably contaminated by the S coda). However, some stations at large distances do not show the T-phase. The ZAFRAN dataset has thus the potential to provide information on T-phase generation and its relation with the sea bottom topography and seawater layering in the Red Sea.

The spectral content of this earthquake is particularly intriguing because of its low-frequency amplitudes. Figures 12b-e show the spectra and the spectrograms for the three closest stations (OBS01, OBS02, and SOUTH, located between 17 and 28 km from the epicenter). The low-frequency content is also highlighted by waveforms for the three closest stations, low-pass filtered at 1 Hz (Figure 12f). This local earthquake is a combination of short-duration high-frequency and long-duration low-frequency events with the low-frequency being recorded first (Figure 12c-e and gray boxes in Figure 12c). These features classify it as a hybrid earthquake and are usually associated with fluid movements and/or conduit resonance due to volcanic or hydrothermal activities (e.g., Chouet, 1996; Neuberg et al., 2000; Leva et al., 2022). However, hybrid events are usually characterized by high-frequency onsets that generate low-frequency resonance of the rocks hosting the fluids (Neuberg et al., 2006). Other studies pointed out that the low-frequency content may be due to deep source or complex path effects (Harrington and Brodsky, 2007; Leva et al., 2022). In the case of the earthquake recorded by the ZAFRAN network, the onset of the low-frequencies is earlier than the onset of the high frequencies, not fitting well with the model that includes the resonance effects after the high-frequency rupture.

Comparison of spectra of signals recorded by the DEPAS OBSs (OBS01 and OBS02) and the Fugro OBS (SOUTH) reveals that the DEPAS OBSs experience resonance at 6 and 10.5 Hz following for at least 150 s after the arrival of the body waves (see Figure 12c-e). SOUTH, instead, does not show these signals. A similar signal at 6 Hz was observed in the DEPAS OBSs by Essing et al. (2021b) and attributed to the vibrations of the radio antenna.

4.4 Teleseismic waveforms

We conduct a qualitative assessment of waveform quality in the long-period range using a 2.5-hour-long time window that displays two Mw 6.7 teleseismic earthquakes. These earthquakes are detectable in spectrograms shown in Figure 7 (see the red box "TL") and are listed in all global earthquake catalogs. They occurred approximately at the same epicentral distance of 73^o but had different back-azimuths (Figure 13a). Their origin times differ by an hour. Band-passed waveforms between 5 and 100 s are displayed in Figure 13b.

Despite the high self-noise of the CMG-40T-OBS sensors in the DEPAS OBSs, the waveform quality for these two earthquakes is generally good, particularly on the vertical components. However, the noise in the horizontal components of some DEPAS OBSs makes it difficult to recognize the arrivals of different phases (Figure 13b, gray waveforms). This is the case for OBS01, OBS02, OBS06, and OBS11. Although the overall median noise

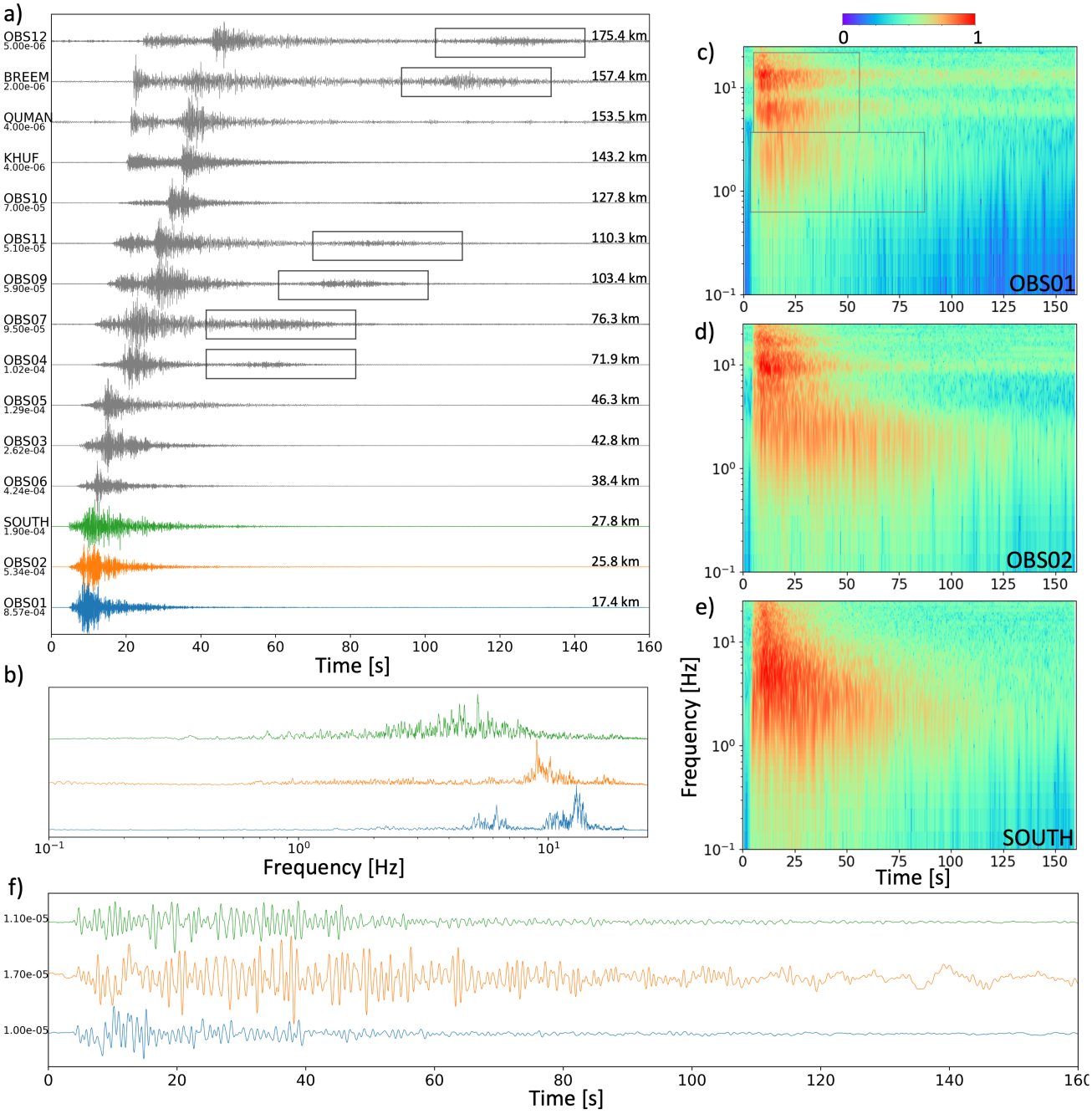

Figure 12 The M_L 3.4 local hybrid earthquake. a) Vertical-component velocity seismograms and highpass filtered at 0.1 Hz. The maximum amplitude in m/s for each waveform is shown below the station's name. Possible T-phases are enclosed in the gray boxes. b) Normalized power spectra of the waveforms in stations OBS01, OBS02, and SOUTH (time window and colors as in a)). c) Normalized spectrograms for the station OBS01. Gray boxes highlight the short-duration high-frequency event and the long-duration low-frequency event. d) and e) as in c) but for OBS02 and SOUTH, respectively. f) Vertical-component velocity seismograms and low-pass filtered at 1 Hz. Colors and units as in a). The location of the earthquake is shown in Figure 1.

level of component 2 of OBS06 is not significantly higher than that of most other DEPAS OBSs (Figure 6), Figure 9 shows that in March 2022, the noise level on component 2 of OBS06 was almost 10 dB higher than the full deployment median. Instead, the overall median noise levels for horizontal component 2 of OBS01, OBS02, and OBS11 are generally higher than in the other stations, so their low waveform quality for these events is expected. The horizontal component waveforms of OBS03 began to exhibit noise at the end of the second earthquake, suggesting a possible temporary malfunction.

The land stations recorded the events excellently across all components (Figure 13b). The Fugro OBS SOUTH recorded the two events in the vertical component with a quality comparable to that of the onshore stations and in the horizontal component with a quality comparable to the average of the DEPAS OBSs.

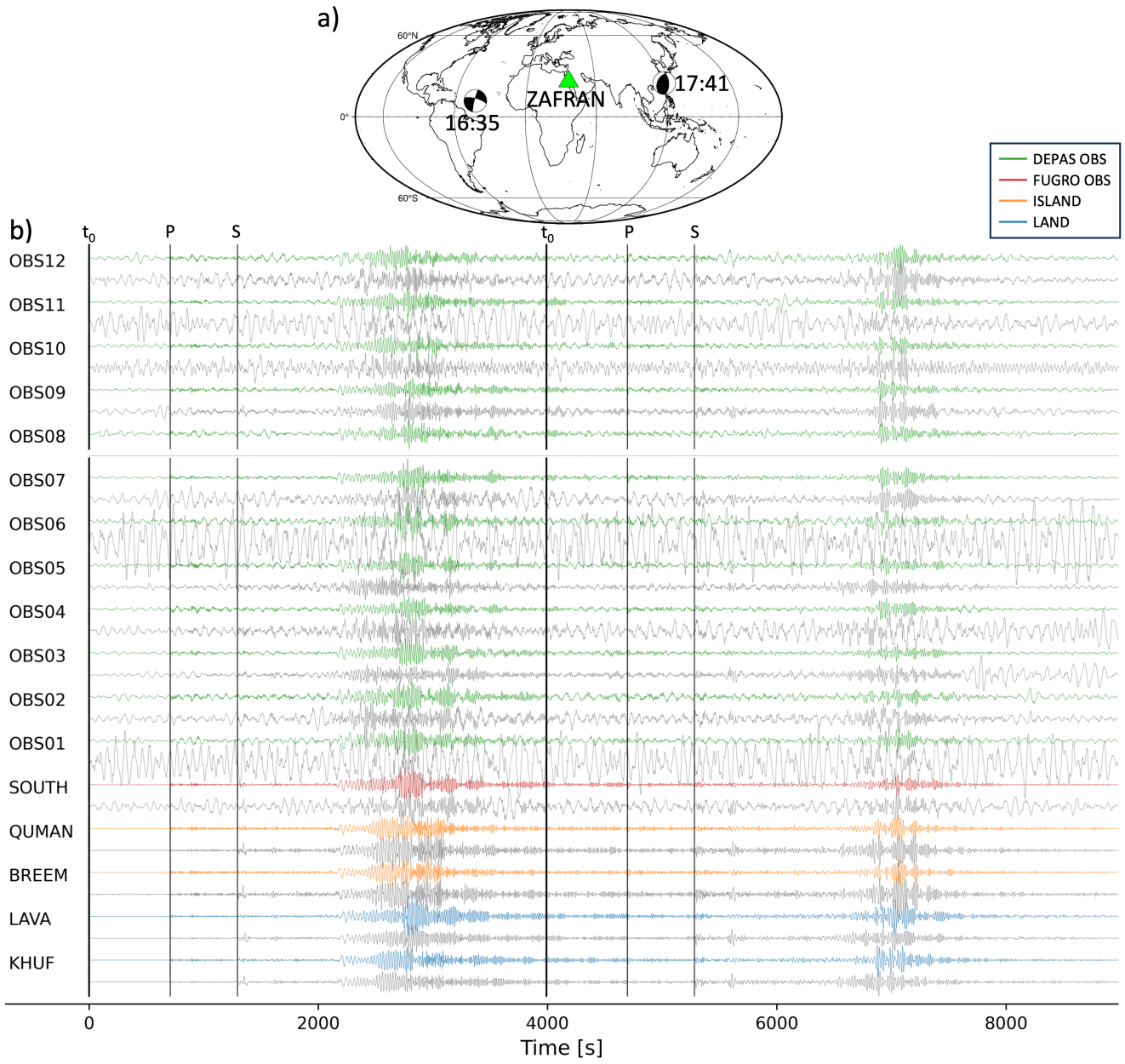

Figure 13 Example of two teleseismic earthquakes. a) Location and focal mechanisms for two M_w 6.7 teleseismic earthquakes that occurred on 22 March 2022 (t_0 displayed next to the focal mechanism). These events are recorded at approximately the same epicentral distance of 73^o. b) 5-100 s bandpass filtered velocity waveforms for the teleseismic earthquakes in a). Vertical seismograms are color-coded as in the legend with the name of the station displayed on the left. 2/E component seismograms are displayed in gray after the corresponding vertical component seismogram. Thick vertical black lines mark the earthquake origin times and thin black lines mark the P and S wave arrivals based on the IASP91 Earth model (Kennet, 1991). Event information is extracted from the Global CMT Catalog (https://www.globalcmt.org, last accessed 5 April 2023).

5 Discussion and conclusions

In this study, we introduce the first OBS deployment in the Red Sea, targeting the seismic activity and the lithospheric structure of the ZFZ. To establish a foundation for seismological investigations incorporating data from the ZAFRAN network, we perform comprehensive data quality control and emphasize notable signals recorded in the ZFZ.

For local seismicity studies, it is important to consider site effects arising from sedimentary and salt coverage since these factors may impact automated methods for determining arrival times and onset polarities on waveforms of local earthquakes. Moreover, in the short-period range, the dataset experiences higher noise levels compared to most global locations (e.g., Stähler et al., 2016, 2018; Hilmo and Wilcock, 2020; Carchedi et al., 2022; Kim et al., 2023; Zhang et al., 2023); this may be attributed to the regular passage of ships, intense seismic or tremor-like activities related to volcanic or hydrothermal phenomena, as suggested by the detection of the hybrid earthquake, or the slow movements of salt coverages resembling glacial creep (Podolskiy et al., 2021). Further disturbances in the short period are due to the strumming of the rope (frequencies larger than 10 Hz) and vibration of other OBS components (frequen-

cies between 6 and 10 Hz).

Several recent studies attempted to model the harmonic noise generated by the head-buoy and rope strumming in the water columns of the DEPAS OBSs (Stähler et al., 2018; Essing et al., 2021b; Corela et al., 2022); however, this was observed at frequencies between 1 and 10 Hz. For example, Stähler et al. (2018) modeled the strumming of the rope and head buoy as it is usually implemented in the Lobsters of the DEPAS pool, including in our deployment. They found that the fundamental frequency of the DEPAS setup's rope is around 1 Hz, roughly corresponding to the shedding frequency of vortices generated by currents at approximately 0.1 m/s (calculated using the formula $f_{vort} = 10.5 \times v$ Hz, with v representing current velocity). Overtones were observed up to 10 Hz. Even considering the potentially higher salinity and temperature of Red Sea water compared to the values used by Stähler et al. (2018), the derivation of the f_{vort} does not change significantly. Consequently, the higher frequencies observed in our dataset suggest sea bottom currents of about 100 cm/s. Currents exceeding 100 cm/s have been documented in selected locations worldwide, such as the Gulf of Mexico and the Strait of Gibraltar, as reported by Shanmugam (2021). Unfortunately, specific sea bottom current data for the Red Sea are unavailable. However, ROV images of the deep Red Sea show that sea-bottom currents are usually weak and not able to blow away light bacterial mats (van der Zwan et al., 2023). These observations imply that either the signal we observe is unrelated to the strumming rope (in this case their occurrence in the OBS with the free rope is by chance only and due to specific locations instead) or the phenomenon interacting with the rope is not a sea bottom current.

In the medium-period range, relevant for example for ambient noise tomography, our analysis of the correlation with the oceanic and atmospheric parameters indicates that local noise sources from wind and waves may adversely affect the quality of noise cross-correlations. Consequently, we recommend utilizing cross-correlations calculated during days of calm local sea states, emphasizing the importance of selecting or weighing cross-correlations using datasets like ERA. The analyses of correlations presented here are extremely important in defining the period range (0.2 - 10 s) of the influence of wind and waves on ambient noise.

In addition, our analyses contribute to a better understanding of a second peak within the medium-period range, occurring at shorter periods than the secondary microseismic peak. The presence of two distinct peaks within the secondary microseismic band is commonly interpreted as occurred due to sources at different distances with the peak at a shorter period generated by local sea conditions and the peak at a longer period due to farther oceanic sources (e.g., Bromirski et al., 2005; Zhang et al., 2023). In our study, the presence of the shorter period peak in the noise of the OBSs and island stations and the lack of the peak in the land stations (see comparison in Figure 5) supports the fact that this shorter period peak is due to local sources whose energy dissipates rapidly inland.

On the other hand, the second peak at a shorter period was also observed in stations located far from the coastline and attributed to and used to retrieve subsurface structure (Parisi et al., 2020; Guo et al., 2021). For example, Kim et al. (2023) also found that the thickness of sediments below the OBSs attenuates (amplifies) periods shorter (longer) than 2 s. In this study, we find that the noise level in the medium-period range correlates well with the sea state, and the correlation functions ρ_{10v} and ρ_{swh} have two peaks at frequencies similar to ones of the noise levels in the medium-period range. Therefore, we would expect that all stations with ρ_{10v} and ρ_{swh} with double peaks should have a double peak noise level, that is, the stations should belong to class A or B. However, we observe that even stations of other classes (no second peak or a large peak including the frequency from the first and second peak), such as OBS12 belonging to class D, have a ρ_{10v} and ρ_{swh} with double peak (see Figure 10). We believe that the shape of the noise level of these stations is due to the effects of the Earth's structure below the station that amplifies some frequencies between the two peaks. Also, the fact that the shape/category of the ZAFRAN stations does not vary in time (Figure 9) further supports the effect of local structure, in addition to the local sources.

The factor significantly affecting the performance of the DEPAS OBS at long-period is the high self-noise levels of the Güralp CMG-40T-OBS sensors, limiting observations in the long-period range (T>10s) in all components (Figure 6). In contrast, the Fugro OBSs, equipped with a Nanometrics Trillium compact sensor, performed as well as the land stations on the vertical component (Figure 6). Noise levels on the horizontal components were comparable in the DEPAS and Fugro OBSs. These findings are consistent with observations made by Stähler et al. (2018) when comparing the two types of sensors installed on Lobsters (the DEPAS OBS configuration). The differences observed in the performances of the OBSs at long periods directly reflect on the quality of waveforms for teleseismic earthquakes. The example in Figure 13 in fact shows the overall good quality of the network with some limitations in some horizontal components of the DEPAS OBS. However, the clear identifications of body and surface waves suggest that the ZAFRAN dataset can be included in global seismology studies for earthquakes of magnitude at least M_w6.7, or less if only the Fugro OBSs are used.

The findings presented in this study hold significance for forthcoming research relying on the ZAFRAN dataset. They bear importance for geological and oceanographic investigations in the Red Sea, as well as for the seismological communities engaged in refining their understanding and use of OBSs.

Acknowledgements

We would like to acknowledge the "German Instrument Pool for Amphibian Seismology (DEPAS)", hosted by the Alfred Wegener Institute Bremerhaven, for providing the OBSs and Fugro for providing access to their OBS dataset. We thank the Coastal and Marine Resource

Core lab of KAUST and in particular Abdullah Mandili, David Atienza, and the crews of the R/V Thuwal and R/V Azizi. We are also grateful to the legal and logistic teams at KAUST and GEOMAR. Moreover, we thank Red Sea Global for supporting our project and providing field support. Lastly, we are grateful to the entire SEISMICA team for their efforts in facilitating the publication of this manuscript, with a special thank to the invaluable feedback provided by the Editor Stephen P. Hicks and two anonymous reviewers, whose comments improved the quality of our work. This research was funded by the KAUST Competitive Research Grant URF/1/4076-01-01.

Data and code availability

Waveforms and instrument responses will be publicly available from the GEOFON data center with network code 5Q after the embargo period (3 years from the end of the deployment). Figure 1 was made with QGIS; Figure 6 with ObsPy (Krischer et al., 2015) and matplotlib; Figures 7,11,12 and 13 with ObsPy. ERA5 datasets are available from ECMWF (European Centre for Medium-Range Weather Forecasts, Hersbach et al., 2023, last access 29 August 2023).

Competing interests

The authors have no competing interests.

References

Alfred-Wegener-Institut Helmholtz-Zentrum für Polar-und Meeresforschung et al., . DEPAS (Deutscher Geräte-Pool für amphibische Seismologie): German Instrument Pool for Amphibian Seismology. *Journal of large-scale research facilities*, 3(A122), 2017. doi: 10.17815/jlsrf-3-165.

Almalki, K. A., Betts, P. G., and Ailleres, L. The Red Sea – 50years of geological and geophysical research. *Earth-Science Reviews*, 147:109–140, 2015. doi: 10.1016/j.earscirev.2015.05.002.

Ardhuin, F. Large-Scale Forces Under Surface Gravity Waves at a Wavy Bottom: A Mechanism for the Generation of Primary Microseisms. *Geophysical Research Letters*, 45(16):8173–8181, 2018. doi: 10.1029/2018GL078855.

Ardhuin, F., Rawat, A., and Aucan, J. A numerical model for free infragravity waves: Definition and validation at regional and global scales. *Ocean Modelling*, 77:20–32, 2014. doi: 10.1016/j.ocemod.2014.02.006.

Augustin, N., van der Zwan, F. M., Devey, C. W., and Brandsdóttir, B. 13 million years of seafloor spreading throughout the Red Sea Basin. *Nature Communications*, 12(1), 2021. doi: 10.1038/s41467-021-22586-2.

Beyreuther, M., Barsch, R., Krischer, L., Megies, T., Behr, Y., and Wassermann, J. ObsPy: A Python Toolbox for Seismology. *Seismological Research Letters*, 81(3):530–533, 05 2010. doi: 10.1785/gssrl.81.3.530.

Blanck, H., Jousset, P., Hersir, G. P., Ágústsson, K., and Ólafur G. Flóvenz. Analysis of 2014–2015 on- and off-shore passive seismic data on the Reykjanes Peninsula, SW Iceland. *Journal of Volcanology and Geothermal Research*, 391:106548, 2020. doi: 10.1016/j.jvolgeores.2019.02.001.

Braunmiller, J., Nabelek, J., and Ghods, A. Sensor Orientation of Iranian Broadband Seismic Stations from P-Wave Particle Motion. *Seismological Research Letters*, 91(3):1660–1671, 04 2020. doi: 10.1785/0220200019.

Bromirski, P. D., Duennebier, F. K., and Stephen, R. A. Mid-ocean microseisms. *Geochemistry, Geophysics, Geosystems*, 6(4), 2005. doi: 10.1029/2004GC000768.

Carchedi, C. J. W., Gaherty, J. B., Webb, S. C., and Shillington, D. J. Investigating Short-Period Lake-Generated Microseisms Using a Broadband Array of Onshore and Lake-Bottom Seismometers. *Seismological Research Letters*, 93(3):1585–1600, 02 2022. doi: 10.1785/0220210155.

Chouet, B. A. Long-period volcano seismicity: Its source and use in eruption forecasting. *Nature*, 380(6572):309 – 316, 1996. doi: 10.1038/380309a0.

Coleman, R. G. and McGuire, A. V. Magma systems related to the Red Sea opening. *Tectonophysics*, 150(1):77–100, 1988. doi: 10.1016/0040-1951(88)90296-X.

Corela, C., Loureiro, A., Duarte, J. L., Matias, L., Rebelo, T., and Bartolomeu, T. The OBS noise due to deep ocean currents. *Natural Hazards and Earth System Sciences Discussions*, 2022:1–21, 2022. doi: 10.5194/nhess-2022-196.

Crawford, W. C. and Webb, S. C. Identifying and Removing Tilt Noise from Low-Frequency (<0.1 Hz) Seafloor Vertical Seismic Data. *Bulletin of the Seismological Society of America*, 90(4):952–963, 08 2000. doi: 10.1785/0119990121.

Delaunay, A., Baby, G., Fedorik, J., Afifi, A. M., Tapponnier, P., and Dyment, J. Structure and morphology of the Red Sea, from the mid-ocean ridge to the ocean-continent boundary. *Tectonophysics*, 849:229728, 2023. doi: 10.1016/j.tecto.2023.229728.

Doran, A. K. and Laske, G. Ocean-Bottom Seismometer Instrument Orientations via Automated Rayleigh-Wave Arrival-Angle Measurements. *Bulletin of the Seismological Society of America*, 107(2):691–708, 01 2017. doi: 10.1785/0120160165.

El-Isa, Z. Seismicity and seismotectonics of the Red Sea Region. *Arabian Journal of Geosciences*, 8(10):8505 – 8525, 2015. doi: 10.1007/s12517-015-1819-2.

Essing, D., Schlindwein, V., Schmidt-Aursch, M. C., Hadziioannou, C., and Stähler, S. C. Characteristics of Current-Induced Harmonic Tremor Signals in Ocean-Bottom Seismometer Records. *Seismological Research Letters*, 92(5):3100–3112, 04 2021a. doi: 10.1785/0220200397.

Essing, D., Schlindwein, V., Schmidt-Aursch, M. C., Hadziioannou, C., and Stähler, S. C. Characteristics of Current-Induced Harmonic Tremor Signals in Ocean-Bottom Seismometer Records. *Seismological Research Letters*, 92(5):3100–3112, 04 2021b. doi: 10.1785/0220200397.

Fittipaldi, M., Trippanera, D., Augustin, N., van der Zwan, Parisi, L., and Jónsson, S. Mabahiss Deep in the Northern Red Sea: New geomorphological insights from high-resolution bathymetric mapping . *Submitted to Geomorphology*, 2024.

Geissler, W. H., Matias, L., Stich, D., Carrilho, F., Jokat, W., Monna, S., IbenBrahim, A., Mancilla, F., Gutscher, M.-A., Sallarès, V., and Zitellini, N. Focal mechanisms for sub-crustal earthquakes in the Gulf of Cadiz from a dense OBS deployment. *Geophysical Research Letters*, 37(18), 2010. doi: 10.1029/2010GL044289.

Gualtieri, L., Stutzmann, E., Capdeville, Y., Ardhuin, F., Schimmel, M., Mangeney, A., and Morelli, A. Modelling secondary microseismic noise by normal mode summation. *Geophysical Journal International*, 193(3):1732–1745, 04 2013. doi: 10.1093/gji/ggt090.

Guo, Z., Huang, Y., and Aydin, A. Double-Frequency Microseisms on the Thick Unconsolidated Sediments in Eastern and Southeastern Coasts of United States: Sources and Applications on Seismic Site Effect Evaluation. *Journal of Earth Science*, 32(5):1190

– 1201, 2021. doi: 10.1007/s12583-021-1426-y.

Hamieh, A., Rowaihy, F., Al-Juaied, M., Abo-Khatwa, A. N., Afifi, A. M., and Hoteit, H. Quantification and analysis of CO2 footprint from industrial facilities in Saudi Arabia. *Energy Conversion and Management: X*, 16:100299, 2022. doi: 10.1016/j.ecmx.2022.100299.

Hannemann, K., Krüger, F., Dahm, T., and Lange, D. Oceanic lithospheric S-wave velocities from the analysis of P-wave polarization at the ocean floor. *Geophysical Journal International*, 207 (3):1796–1817, 09 2016. doi: 10.1093/gji/ggw342.

Harrington, R. M. and Brodsky, E. E. Volcanic hybrid earthquakes that are brittle-failure events. *Geophysical Research Letters*, 34 (6), 2007. doi: 10.1029/2006GL028714.

Heleno, S. I., Faria, B. V., Bandomo, Z., and Fonseca, J. F. Observations of high-frequency harmonic tremor in Fogo, Cape Verde Islands. *Journal of Volcanology and Geothermal Research*, 158 (3):361–379, 2006. doi: 10.1016/j.jvolgeores.2006.06.018.

Hersbach, H., Bell, B., Berrisford, P., Biavati, G., Horányi, A., Muñoz Sabater, J., Nicolas, J., Peubey, C., Radu, R., Rozum, I., Schepers, D., Simmons, A., Soci, C., Dee, D., and Thépaut, J.-N. ERA5 hourly data on single levels from 1940 to present. *Copernicus Climate Change Service (C3S) Climate Data Store (CDS)*, 2023. doi: 10.24381/cds.adbb2d47.

Hilmo, R. and Wilcock, W. S. D. Physical Sources of High-Frequency Seismic Noise on Cascadia Initiative Ocean Bottom Seismometers. *Geochemistry, Geophysics, Geosystems*, 21(10): e2020GC009085, 2020. doi: 10.1029/2020GC009085.

Janiszewski, H. A., Gaherty, J. B., Abers, G. A., Gao, H., and Eilon, Z. C. Amphibious surface-wave phase-velocity measurements of the Cascadia subduction zone. *Geophysical Journal International*, 217(3):1929–1948, 01 2019. doi: 10.1093/gji/ggz051.

Janiszewski, H. A., Eilon, Z., Russell, J. B., Brunsvik, B., Gaherty, J. B., Mosher, S. G., Hawley, W. B., and Coats, S. Broad-band ocean bottom seismometer noise properties. *Geophysical Journal International*, 233(1):297–315, 11 2022. doi: 10.1093/gji/ggac450.

Kennet, B. L. N. IASPEI 1991 SEISMOLOGICAL TABLES. *Terra Nova*, 3(2):122–122, 1991. doi: 10.1111/j.1365-3121.1991.tb00863.x.

Kim, T., Park, J., Ko, J., Oh, S., Witek, M., Chang, S., Lee, S., Kim, Y., Utada, H., Kawakatsu, H., Shiobara, H., Isse, T., Takeuchi, N., and Sugioka, H. Characteristics of Background Noise in the Oldest-1 Array Deployed on the Oldest Part of the Pacific Plate. *Bulletin of the Seismological Society of America*, 113(4):1772–1793, 04 2023. doi: 10.1785/0120220215.

Klein, F. W. User's guide to HYPOINVERSE-2000, a Fortran program to solve for earthquake locations and magnitudes. *USGS, Open-File Report 2002-171*, 2002.

Krischer, L., Megies, T., Barsch, R., Beyreuther, M., Lecocq, T., Caudron, C., and Wassermann, J. ObsPy: a bridge for seismology into the scientific Python ecosystem. *Computational Science & Discovery*, 8(1):014003, may 2015. doi: 10.1088/1749-4699/8/1/014003.

Leva, C., Rümpker, G., and Wölbern, I. Multi-array analysis of volcano-seismic signals at Fogo and Brava, Cape Verde. *Solid Earth*, 13(8):1243–1258, 2022. doi: 10.5194/se-13-1243-2022.

Marshak, S., Bonatti, E., Brueckner, H., and Paulsen, T. Fracture-zone tectonics at Zabargad Island, Red Sea (Egypt). *Tectonophysics*, 216(3):379–385, 1992. doi: 10.1016/0040-1951(92)90407-W.

McNamara, D. E. and Buland, R. P. Ambient Noise Levels in the Continental United States. *Bulletin of the Seismological Society of America*, 94(4):1517–1527, 08 2004. doi: 10.1785/012003001.

Naranjo, D., Parisi, L., Jónsson, S., Jousset, P., Werthmüller, D., and Weemstra, C. Ocean Bottom Seismometer Clock Correction using Ambient Seismic Noise. *Seismica*, 3(1), Jan. 2024. doi: 10.26443/seismica.v3i1.367.

Neuberg, J., Luckett, R., Baptie, B., and Olsen, K. Models of tremor and low-frequency earthquake swarms on Montserrat. *Journal of Volcanology and Geothermal Research*, 101(1):83–104, 2000. doi: 10.1016/S0377-0273(00)00169-4.

Neuberg, J., Tuffen, H., Collier, L., Green, D., Powell, T., and Dingwell, D. The trigger mechanism of low-frequency earthquakes on Montserrat. *Journal of Volcanology and Geothermal Research*, 153(1):37–50, 2006. doi: 10.1016/j.jvolgeores.2005.08.008.

Okal, E. A. The generation of T waves by earthquakes. volume 49 of *Advances in Geophysics*, pages 1–65. Elsevier, 2008. doi: 10.1016/S0065-2687(07)49001-X.

Parisi, L., Stanistreet, I., Njau, J., Schick, K., Toth, N., and Mai, P. M. Seismological Investigations in the Olduvai Basin and Ngorongoro Volcanic Highlands (Western Flank of the North Tanzanian Divergence). *Seismological Research Letters*, 91(6):3286–3303, 09 2020. doi: 10.1785/0220200111.

Peterson, J. Observations and Modeling of Seismic Background Noise. *U.S. Geological Survey open-file report*, Albuquerque, N.M:93–3222, 1993. doi: 10.1016/j.ocemod.2014.02.006.

Podolskiy, E. A., Murai, Y., Kanna, N., and Sugiyama, S. Ocean-bottom and surface seismometers reveal continuous glacial tremor and slip. *Nature Communications*, 12(1), 2021. doi: 10.1038/s41467-021-24142-4.

Rehman, F., Alamri, A. M., El-Hady, S. M., Harbi, H. M., and Atef, A. H. Seismic hazard assessment and rheological implications: a case study selected for cities of Saudi Arabia along the eastern coast of Red Sea. *Arabian Journal of Geosciences*, 10(24), 2017. doi: 10.1007/s12517-017-3325-1.

Schlindwein, V., Krüger, F., and Schmidt-Aursch, M. Project KNIPAS: DEPAS ocean-bottom seismometer operations in the Greenland Sea in 2016-2017, 2018. doi: 10.1594/PANGAEA.896635.

Shanmugam, G. Chapter 8 - Bottom currents. In Shanmugam, G., editor, *Mass Transport, Gravity Flows, and Bottom Currents*, pages 309–375. Elsevier, 2021. doi: 10.1016/B978-0-12-822576-9.00008-4.

Stutzmann, E., Roult, G., and Astiz, L. GEOSCOPE Station Noise Levels. *Bulletin of the Seismological Society of America*, 90(3): 690–701, 06 2000. doi: 10.1785/0119990025.

Stähler, S., Sigloch, K., Hosseini, K., Crawford, W., Barruol, G., Schmidt-Aursch, M., Tsekhmistrenko, M., Scholz, J.-R., Mazzullo, A., and Deen, M. Performance report of the RHUM-RUM ocean bottom seismometer network around la Réunion, western Indian Ocean. *Advances in Geosciences*, 41:43 – 63, 2016. doi: 10.5194/adgeo-41-43-2016.

Stähler, S. C., Schmidt-Aursch, M. C., Hein, G., and Mars, R. A Self-Noise Model for the German DEPAS OBS Pool. *Seismological Research Letters*, 89(5):1838–1845, 08 2018. doi: 10.1785/0220180056.

Trabattoni, A., Barruol, G., Dréo, R., and Boudraa, A. Ship detection and tracking from single ocean-bottom seismic and hydroacoustic stations. *The Journal of the Acoustical Society of America*, 153(1):260–273, 01 2023. doi: 10.1121/10.0016810.

van der Zwan, F. M., Augustin, N., Petersen, S., Altalhi, S. M., Schultz, J., Peixoto, R. S., Follmann, J., Anker, A., Benzoni, F., Garcia Paredes, E. R., Al Malallah, M., Shepard, L., Ouhssain, M., Jägerup, S. B., Jones, B. H., and Rosado, A. S. Widespread diffuse venting and large microbial iron-mounds in the Red Sea. *Communications Earth and Environment*, 4(1), 2023. doi: 10.1038/s43247-023-01169-7.

Wilcock, W. S. D. Tracking fin whales in the northeast Pacific Ocean with a seafloor seismic network. *The Journal of the Acoustical Society of America*, 132(4):2408–2419, 10 2012. doi: 10.1121/1.4747017.

Zhang, H., Schmidt-Aursch, M. C., Geissler, W. H., and Xing, J. Characteristics of the Oceanic Ambient Seismic Noise Around Tristan da Cunha in the South Atlantic From OBS Data. *Journal of Geophysical Research: Solid Earth*, 128(6):e2022JB025884, 2023. doi: 10.1029/2022JB025884.